약학박사학위논문

Role of AKAP12 and Claudin5 in Kupffer's vesicle development

Kupffer's vesicle 발생 과정에서 AKAP12 와 Claudin5 의 역할 연구

2017 년 8 월

서울대학교 융합과학기술대학원

분자의학 및 바이오제약학과

김 정 균

Role of AKAP12 and Claudin5 in Kupffer's vesicle development

Kupffer's vesicle 발생 과정에서 AKAP12 와 Claudin5 의 역할 연구

지도교수 서 영 준

이 논문을 약학박사 학위논문으로 제출함
2017년 6월

서울대학교 융합과학기술대학원
분자의학 및 바이오제약학과
김 정 균

김정균의 약학박사 학위논문을 인준함
2017년 6월

위 원 장 _____ (印)

부위원장 _____ (印)

위 원 _____ (印)

위 원 _____ (印)

위 원 _____ (印)

ABSTRACT

Role of AKAP12 and Claudin5 in Kupffer's vesicle development

Jeong-gyun Kim

Department of Molecular Medicine and Biopharmaceutical Science
Graduate School of Convergence Science and Technology
Seoul National University

Left-right asymmetric organ development is important to establish a proper body plan of vertebrates. In zebrafish, the Kupffer's vesicle (KV) is a fluid-filled sac which controls asymmetric organ development, and a properly inflated KV lumen by means of fluid influx is a prerequisite for the asymmetric signal transmission. KV is derived from the dorsal forerunner cells (DFCs), which collectively migrate from the margin of the embryonic shield to the tail bud region, and become polarized to form a rosette structure. Then, the lumen is formed at the apical point of the rosette structure and expanded by fluid influx through ion channels. Finally, nodal signal is exclusively restricted in left-lateral plate mesoderm and organ shows its laterality. However, the underlying mechanisms of the cell-cell interaction during KV formation are poorly studied. Here, I identified that *akap12* was expressed in DFCs and downregulation of *akap12β* in zebrafish showed a failure in organ laterality that resulted from

malformed KV. In addition, KV lineage cell-specific knockdown of *akap12β* also exhibited the organ laterality defects. In *akap12β* morphants, cluster of DFC was fragmented which represents a failure of cell collectivity within DFCs, and Cdh1 expression was decreased. Thus, these findings suggest that *akap12β* regulates KV development by maintaining cell collectivity within DFCs via Cdh1-mediated adherens junction. Furthermore, I identified that the *cldn5a* is highly expressed at the apical surface of KV epithelial cells and tightly seals the KV lumen. Downregulation of *cldn5a* in zebrafish showed a failure in organ laterality that resulted from malformed KV. In addition, accelerated fluid influx into KV by combined treatment of forskolin and 3-isobutyl-1-methylxanthine failed to expand the partially-formed KV lumen in *cldn5a* morphants. However, malformed KV lumen and defective heart laterality in *cldn5a* morphants were significantly rescued by exogenous *cldn5a* mRNA, suggesting that the tightness between the luminal epithelial cells is important for KV lumen formation. Thus, these findings suggest that *cldn5a* is required for KV lumen inflation and left-right asymmetric organ development. Taken together, these findings suggest that *akap12β* regulates KV development by maintaining cell collectivity within DFCs via Cdh1-mediated adherens junction and *cldn5a* regulates KV development by tight sealing the paracellular space between the KV epithelial cells.

Keywords : AKAP12; Claudin5; Kupffer's vesicle; Dorsal forerunner cells; collective cell migration; lumen formation; zebrafish

***Student Number* : 2013-31372**

TABLE OF CONTENTS

LIST OF FIGURES

LIST OF TABLES

LIST OF ABBREVIATIONS

AC; adenylyl cylase

AKAP; A-kinase anchoring protein

BAC; bacterial artificial chromosome

cAMP; cyclic adenosine monophosphate

CaMK; calmodulin kinase

Cas9; CRISPR-associated system CDS; coding sequence

CNS; central nervous system

CFTR; cystic fibrosis conductance regulator

CRISPR; Clustered regularly interspaced short palindromic repeats

DAB; 3,3'-diaminobenzidine

DIC; differential interference contrast

DFC; dorsal forerunner cell

DMSO; dimethyl sulfoxide

ECL; extracellular loop

EDTA; Ethylenediaminetetraacetic acid

EVL; enveloping layer

GFP; green fluorescent protein

HA; homology arm

HDR; homology directed repair

hpf; hours post-fertilization

IBMX; 3-isobutyl-1-methylxanthine

ISH; *in situ* hybridization

KV; Kupffer's vesicle

LRO; left-right organizer

M-MLV; moloney murine leukaemia virus

MO; morpholino oligomer

NBT/BCIP; nitrobuleterazolium/5-bromo, 4-chloro, 3-indolylphosphate

NLS; nuclear localization sequence

PBDTT; 1X PBS, 0.1% Tween 20, 1% DMSO, and 0.5% Triton X-100

PBS; phosphate-buffered saline

PFA; paraformaldehyde

PKA; protein kinase A

PKC; protein kinase C

Prim-5; primordium 5

ROCK; Rho-associated protein kinase

Q-PCR; quantitative-polymerase chain reaction

RT-PCR; reverse transcription polymerase chain reaction

ss; somite stage

TALEN; transcription activator-like effector nucleases

WT; wild-type

ZO-1; zonula occluden-1

INTRODUCTION

1. Organ laterality and left-right organizer

The internal organs, such as the heart, pancreas, and liver, are asymmetrically located along the midline of the body even though the external body plane of vertebrates seems symmetric. Heart, spleen and stomach are located on the left, in contrast to liver which is on the right. However, about 1.1 per 10000 of new born babies in every year showed failures of left-right asymmetric organ development, *situs inversus totalis* or *situs ambiguous* (Lin et al., 2014). Different from the normal position of organ, *situs solitus*, *situs inverus totalis* shows the complete mirror image of normal organ and *situs ambiguous* shows variety form of disrupted organ laterality (Fig. 1) (Fliegauf et al., 2007). A fourth of patient with laterality defects also suffer from primary ciliary dyskinesia, a dysfunction of the cilia in respiratory tract, sperm cells, or fallopian tube (Ceccaldi et al., 2004; McComb et al., 1986). This high correlation between ciliary function and laterality defect enabled the discovery of the existence of left-right organizer (LRO), a transient ciliary organ which controls left-right asymmetric development in vertebrate. The node in mice, gastrocoel roof plate in *Xenupus*, Hensen's node in chick, and Kupffer's vesicle in zebrafish were identified as LROs and they show similar but distinct shapes and sizes, ranging from flat to indented, dome-shaped to spherical, depending on the model organisms (Fig. 2) (Nakamura and Hamada, 2012).

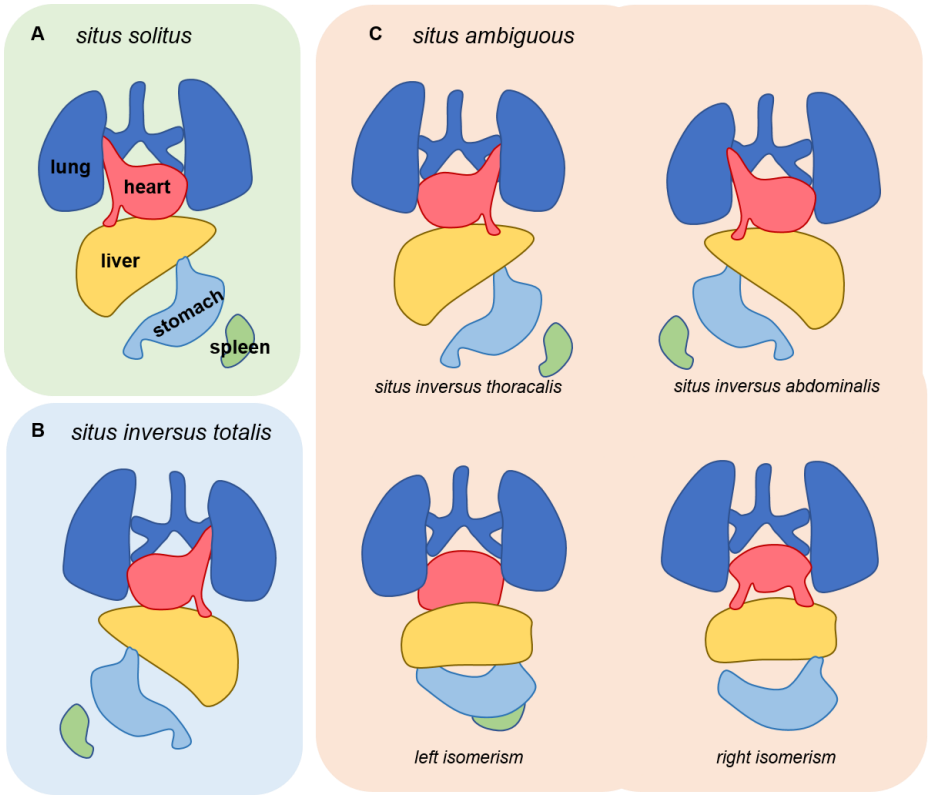

Figure 1. Left-right asymmetry.

(A-C) Illustration of *situs solitus* (A), *situs inversus totalis* (B) and *situs ambiguous* (C).

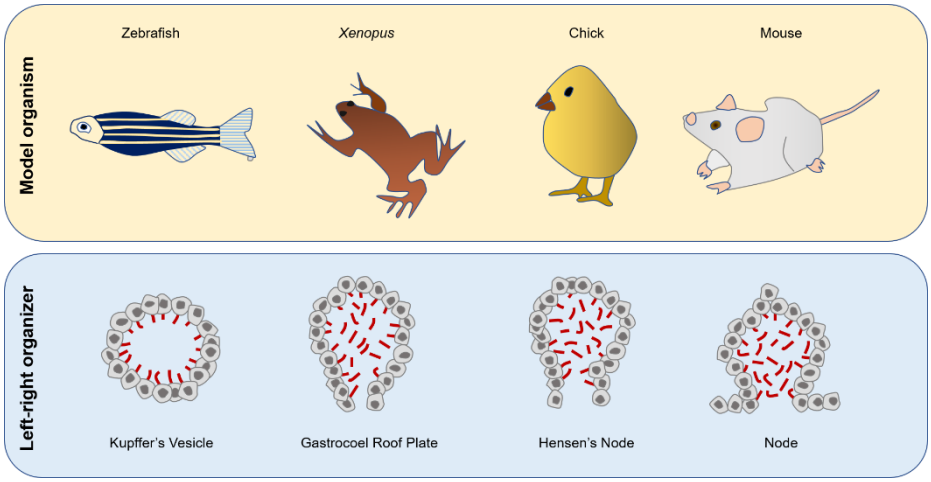

Figure 2. Left-right organizer in several vertebrates.

Illustration of left-right organizer in zebrafish (Kupffer's vesicle), *Xenopus* (Gastrocoel Roof Plate), chick (Hensen's node) and mouse (Node).

2. Kupffer's vesicle development

KV, discovered in 1868, is a distinctive fluid-filled epithelial sac and exists transiently during the early segmentation period at the posterior end of the notochord in zebrafish (Amack and Yost, 2004; Essner et al., 2005). KV is derived from a cluster of dorsal forerunner cells (DFCs), which is maintained by cadherin-based adherens junction, and actively migrates towards the vegetal pole showing filopodia and lamellipodia and passively adheres to the overlying surface enveloping layer (EVL) until planar cell polarity signaling reconstructs the cell structure (Ablooglu et al., 2010; Amack and Yost, 2004; Essner et al., 2005; Matsui et al., 2015; Oteiza et al., 2008; Oteiza et al., 2010). In addition, DFCs are prevented from intermingling with neighboring non-DFCs by Eph/ephrin signaling (Zhang et al., 2016). Then, migrated DFCs become polarized to form a rosette-like structure and the lumen forms at the apical point of the rosette structure (Oteiza et al., 2008). The KV lumen is expanded by fluid influx and ciliogenesis occurs simultaneously with lumen expansion inside KV (Ellertsdottir et al., 2006; Essner et al., 2005; Kramer-Zucker et al., 2005; Navis et al., 2013; Oishi et al., 2006; Roxo-Rosa et al., 2015). In addition, together with *rock2b*-mediated cytoskeletal rearrangement, the notochord affects regional cell shape changes by the accumulation of extracellular matrix (Compagnon et al., 2014; Wang et al., 2011; Wang et al., 2012). Thus, cilia are more abundantly distributed on the anterior-dorsal region. Motile monocilia generate fluid flow in the counterclockwise direction and promote Ca^{2+}

elevation at the left side of the KV via the membrane-targeted calmodulin-dependent protein kinase (CaMK)-II, Pkd2, and Ryr3 (Bisgrove et al., 2005; Francescatto et al., 2010; Jurynec et al., 2008; Schottenfeld et al., 2007). Then, *dand5*, which is a member of the Cerberus/Dan family and antagonizes Spaw function, is expressed bilaterally around the KV lumen at 6 ss and later becomes predominant on the right side (Hashimoto et al., 2004; Lopes et al., 2010). Thus, Spaw, a *nodal*-related protein, is transmitted through the left lateral plate mesoderm, and midline molecular barriers restrict Spaw expression to the left side (Lenhart et al., 2011; Long et al., 2003; Smith et al., 2011; Wang and Yost, 2008). Finally, *nodal* signaling induces left-right asymmetric organ development from organ primordia (Baker et al., 2008; de Campos-Baptista et al., 2008; Horne-Badovinac et al., 2003).

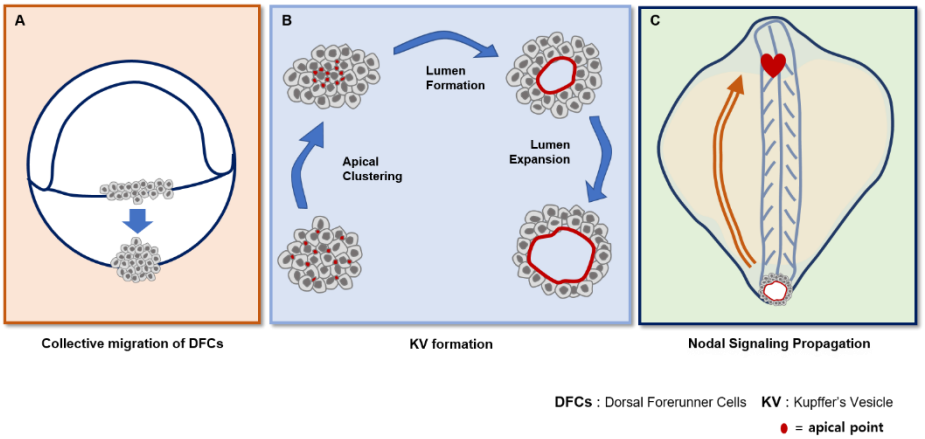

Figure 3. Illustration of KV development and organ laterality determination.

(A) Collective migration of DFCs from shield to bud stage. (B) KV formation from DFCs. (C) Exclusive expression of *spaw* in left-lateral plate mesoderm and heart laterality.

3. A-Kinase Anchoring Protein 12 (AKAP12)

A-kinase anchoring protein12 (AKAP12) is a member of AKAP family which have a binding domain for regulatory subunit of protein kinase A (PKA) and localize holoenzyme to the specific location within the cell. Beside the PKA, AKAP12 displays diverse docking sites for protein kinase C (PKC), calmodulin, cyclins, β-1,4-galactosyltranferase, protein phosphatases, the non-receptor tyrosine kinase Src, and β_2-adrenergic receptor. In addition, AKAP12 encodes three polybasic domains, four nuclear localization signals (NLS), and a nuclear exclusion domain. Therefore, AKAP12 has various functions in many biological processes including cell migration, cell cycle regulation, barriergenesis, tumor progression and wound healing process.

Especially, it is reported that AKAP12 attenuates neovascularization and stabilizes the blood-brain barrier (Lee et al., 2003). AKAP12 stimulates angiopoietin-1 expression in astrocytes and decreases the expression of vascular endothelial growth factor. In addition, conditioned media from AKAP12-overexpressing astrocyte increases tight junction proteins in endothelial cells. This barriergenetic property of AKAP12 is also applied to the repair process after central nervous system (CNS) injury. AKAP12 is strongly expressed in the fibrotic scar during the CNS repair process and AKAP12 knockout mice showed the relatively less tight junction protein expressions which enable the structure to function as a physical barrier (Cha et al., 2014). Recently, it is also reported that PKA compartmentalization via AKAP12 affects the maintenance of the endothelial barrier (Radeva et al., 2014).

In zebrafish, *akap12* is involved in mesodermal cell shape change, muscle progenitor cell migration and regulation of vascular integrity (Kim et al., 2014;

Kwon et al., 2012; Weiser et al., 2007). Interestingly, the previous studied of *akap12* in zebrafish did not focus on the difference of the two isoforms of *akap12*. Although the two isoforms of *akap12, akap12α* and *akap12β,* have a common large exon of *akap12* which comprises 95.6% of the *akap12α* isoform and 99.5% of the *akap12β* isoform, respectively and only differ at small part of N-termini region, *akap12α* and *akap12β* have independent promoters and show distinct mRNA expressions during embryogenesis (Kwon et al., 2012; Streb et al., 2004). Thus, I postulate that there be a distinct function between the *akap12α* and *akap12β* during zebrafish embryonic development.

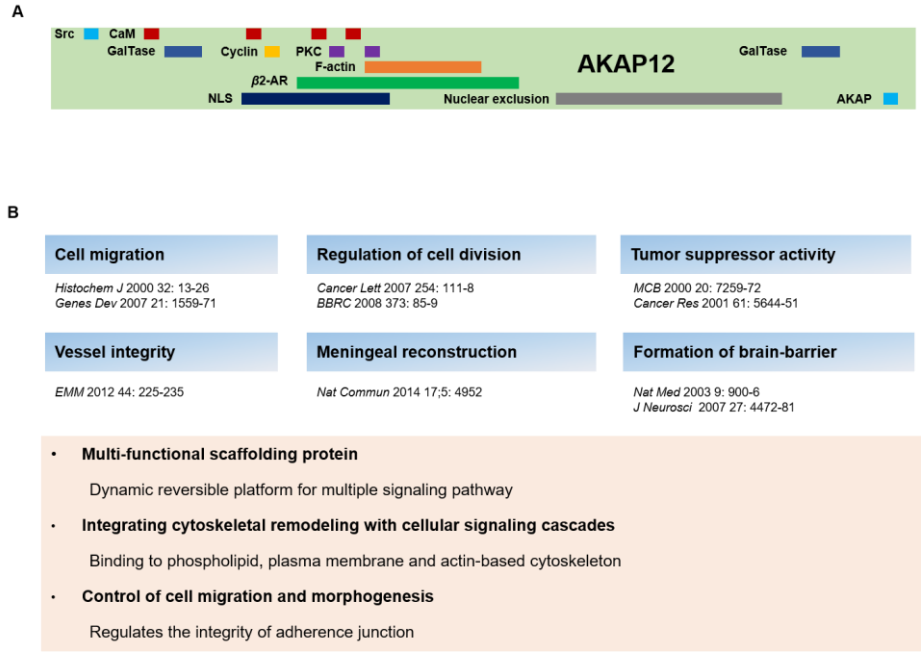

Figure 4. Diverse roles of AKAP12.

(A) Multiple binding domains for signaling molecules. (B) Various functions of AKAP12

4. Tight junction and Claudin5

In multicellular organism, neighboring cells in specific part of organ are tightly adhered to restrict the movement of molecules. This paracellular junction is formed by tight junction, adherens junction and desmosome (Cereijido et al., 2004; Farquhar and Palade, 1963). Tight junction, which is essential for establishment of epithelial and endothelial barriers, and regulating paracellular diffusion of water-soluble molecules between the adjacent cells, is composed of trasmembrane proteins, including claudin and occludin, and cytoplasmic adaptor proteins such as Zonula occludens-1 (ZO-1) (Zihni et al., 2016).

Claudins are the key integral proteins which have a critical role in supporting tight junctions and twenty-four members of the claudin family have been identified in mammals (Jia et al., 2014). Cldn5 is the dominant type in the brain endothelial cells, which maintains the blood-brain barrier permeability, and the loss of Cldn5 in mice showed the size-selective loosening of the blood-brain barrier (Cooper et al., 2011; Jeong et al., 2008; Nitta et al., 2003; Ohtsuki et al., 2007; Ohtsuki et al., 2008).

In zebrafish, *cldn5a* expression in CNS and its role in regulating paracellular tightness of the cerebral ventricular barrier was reported (Zhang et al., 2010). However, the previous study only focus on the CNS region and did not examine the serial expression of *cldn5a* during embryogenesis. Here, I discovered the *cldn5a* expression at the apical surface of KV lumen and investigated the role of *cldn5a* in KV development.

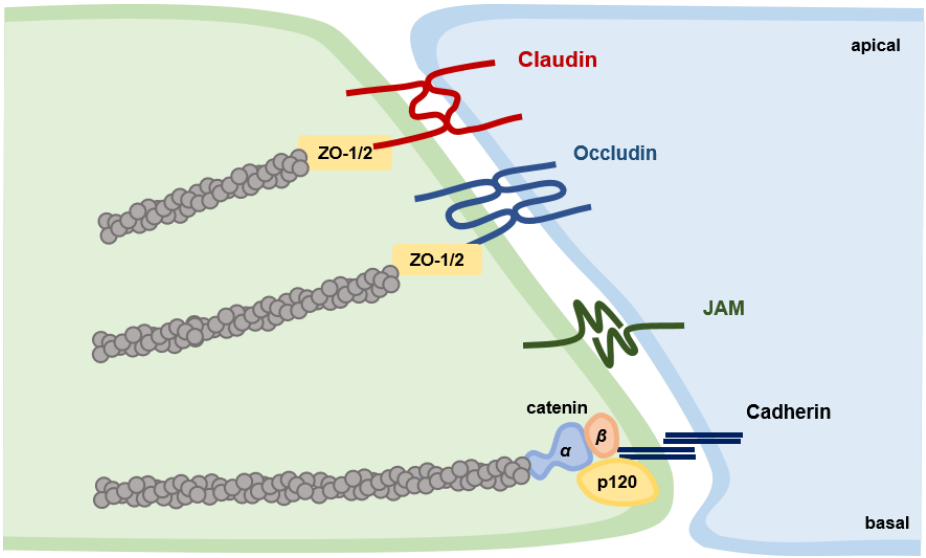

Figure 5. Cell-cell junction and intercellular junction components.

Illustration of cell-cell junction and constituents including ZO-1, Occludin, Claudin, JAM, Catenin, and Cadherin.

PURPOSE OF THIS STUDY

KV is a fluid-filled epithelial sac that regulates left-right asymmetric organ development in zebrafish. From collective migration of DFCs to the establishment of KV lumen, neighboring cells are adhered together and show cooperative behavior. Cluster of DFCs, which collectively migrate from the margin of the embryonic shield to the tail bud region, is maintained by *fgf* feedback loop and Cdh1-mediated adherens junction. Thus, I speculated that AKAP12, which is expressed in non-mesodermal cells within the lateral margin and has important roles in cell motility and junctional protein regulation, might be involved in collective migration of DFCs. Furthermore, KV epithelial cells should be adhered together tightly to sustain hydrostatic pressure during the KV lumen expansion. It is only found that ZO-1, the cytoplasmic scaffold protein that anchors tight junction proteins to the cytoskeleton, is expressed at the apical point of KV epithelial cells. Thus, the presence of the functional tight junction protein, which constitutes and tightly seals the intercellular spaces of KV epithelial cells during apical clustering and lumen inflation need to be investigated. Here, I revealed that *cldn5a* is expressed in KV lineage cells and its role in KV development.

MATERIALS AND METHODS

1. Ethics statement

All zebrafish work was carried out in accordance with protocols approved by the Institutional Animal Care and Use Committees of Seoul National University.

2. Zebrafish

Tuebingen wild-type zebrafish was obtained from the Zebrafish International Resource Center (Oregon, USA), and *Tg(sox17:egfp)* zebrafish embryo was obtained from Zebrafish Organogenesis Mutant Bank (Daegu, Korea).

3. Reverse Transcription-Polymerase Chain Reaction

RNA was isolated using Trizol reagent (Invitrogen). To establish cDNA library, RNA was reverse transcribed using M-MLV Reverse Transcriptase (Promega). The polymerase chain reaction (PCR) conditions were as follows: for *cldn5a*, 28 cycles at 94°C for 45 sec, 60°C for 45 sec, 72°C for 1 min; for *cldn5b*, 32 cycles at 94°C for 45 sec, 60°C for 45 sec, 72°C for 1 min; for *actβ2*, 18 cycles at 94°C for 45 sec, 60°C for 45 sec, 72°C for 1 min, for *akap12* mutant confirmation, 36 cycles at 94°C for 30 sec, 66°C for 30 sec, 68°C for 40 sec. Specific primer pairs are described in table 2.

4. Quantitative-PCR

Target-specific primer pair, cDNA and SyBr Master Mix were prepared for reaction. The reaction conditions were as follows: initial denaturation at 95’C for 10min, 40 cycles of denaturation at 95’C for 15sec, annealing at 55’C for 30sec and elongation at 72’C for 30sec. PCR reaction was performed using

StepOnePlus real-time PCR system (Applied Biosystems). Specific primer pairs are described in table 2.

5. Morpholino injection

For global knockdown, antisense morpholino oligomer (MO) were injected into the yolk at one-cell stage. For specific-knockdown at DFCs, MOs were injected into the yolk at 128-cell to high stage. MOs were purchased from Gene Tools, LLC. Sequence of each MOs are as follows: standard control MO (5'-CCT CTT ACC TCA GTT ACA ATT TAT A-3'), *akap12α* splicing blocking MO (5'-TAC CTT GCC ATC TGC GGT TTC TCC A-3'), *akap12β* splicing blocking MO (5'-TCT TAC CTG TTA GAG TTA TTG TCC C-3'), *cdh1* translation blocking MO (5'-ATC CCA CAG TTG TTA CAC AAG CCA T-3'), *cldn5a* translation blocking MO1 (5'-GTA CTA AAA GGA GTT TAG AAG TTT G-3'), and *cldn5a* translation blocking MO2 (5'-AGG CCA TCG CTT TCT TTT CCC ACT C-3').

6. Pharmacological Reagents

Forskolin and 3-isobutyl-1-methylxanthine (IBMX) were purchased from Sigma-Aldrich (F6886, I7018). Each reagent was primarily stocked for 10 mM and 100 mM in dimethyl sulfoxide (DMSO), respectively. Embryos were treated with the mixture of 10 μM forskolin and 40 μM IBMX from 90% epiboly to 6 somite stage.

7. *In vitro* transcription

PCR-amplified *cldn5a* and *akap12β* were cloned into pCS2^{+} vector. 5'-capped and poly(A)-tailed mRNAs were generated using mMessage mMachine ultra

kit (Ambion). 80-120pg of *akap12β* or *cldn5a* mRNA were co-injected with MO. Primer sequences for PCR amplification were as below: *akap12β* forward (5'-CAA GAA TTC CAT GCT TGG GAC AAT AAC TCT AAC A-3') and reverse (5'-CAA TCT AGA TCA TGA CAC TGT GAC AAC CTC TGT G-3'), *cldn5a* forward (5'-CAA GAA TTC CAT GGC CTC CGC GGC TTT GGA-3') and reverse (5'-CAA TCT AGA TCA CAC GTA ATT CCT CTT GT-3').

8. Transgenesis of *Tg(akap12β:mCheery-caax)*

Method was following the previously described protocol (Bussmann and Schulte-Merker, 2011). Primers for transgenesis are described in table 3.

9. Genome editing using CRISPR/Cas9 system

From cloning gRNA vector constructs to *in vitro* transcription, detailed protocol was following the method as described in the previous report (Jao et al., 2013). For generation of *cldn5a*-targeting gRNA constructs, two pairs of oligonucleotides, gRNA1 forward (5'-TAG GTC TGA TCC TGT GCG TCT G-3') and reverse (5'-AAA CCA GAC GCA CAG GAT CAG A-3'), and gRNA2 forward (5'-TAG GTC TGC GCG ACC ACG ATG T-3') and reverse (5'-AAA CAC ATC GTG GTC GCG CAG A-3'), were annealed and incorporated into BsmBI-digested pT7-gRNA (Addgene plasmid #46759), respectively.

10. genomic DNA isolation.

To isolate genomic DNA, amputated adult zebrafish tail fin or zebrafish embryos were incubated with SNET buffer (20 mM Tris-HCl, 400 mM NaCl, 400 μg/mL proteinase K, 5 mM ethylenediaminetetraacetic acid [EDTA], 1%

sodium dodecyl sulfate [SDS], pH 8.0) at 55℃ for overnight. Then, equal volume of PCI solution [phenol: chloroform: isoamyl alcohol] was added to the gDNA containing SNET buffer, and the organic and aqueous phases were separated by centrifugation of the samples at 666g for 5min. Supernatant was transferred to the new tube, and the gDNA was precipitated by adding an equal volume of isopropanol. After collecting the precipitated gDNA by centrifugation at 13,250g for 15min at 4℃, carefully removed the isopropanol and rinsed the pellet of gDNA with 1mL of 70% ethanol. Then, the pellet was dried for 20 min, and gDNA pellet was dissolved in nuclease free water.

11. T7E1 analysis

Wild-type (WT) and mutant gDNA amplicons were melted and reannealed to hybridize DNA strand randomly. Then, the gDNA was incubated with T7E1 restriction enzyme for 15 min at 37℃.

12. AlwN1 restriction analysis

akap12 WT and mutant gDNA amplicons were incubated with AlwN1 restriction enzyme for 3 hours at 37℃.

13. Melting temperature analysis

akap12 WT and mutant gDNA amplicons were gradually warmed from 60℃ to 95℃. Then, the relative amount of remaining SyBr reporter signal was continuously measured in StepOnePlus instrument.

14. Whole-mount i*n situ* hybridization

Specific regions for *cmlc1, spaw, dand5, foxj1a, cldn5a* and *cldn5b* were

cloned into pGem-T easy vector (Promega). *akap12* probe vector was previously described (Kim et al., 2014). Constructed vectors were linearized and transcribed using DIG-labeling mix, SP6, T7 RNA polymerase (Roche). The embryos were fixed with 4% paraformaldehyde (PFA) for overnight at 4℃ and dehydrated with methanol at –20℃ for long storage. Then, the embryos were treated with proteinase K for 1 to 10 min at room temperature depending on the developmental stages. After the proteinase K treatment, the embryos were transferred to the pre-hybridization solution (50% formamide, 5X Sodium Saline Citrate [SSC], 5 mg/mL yeast tRNA, 50 μg/mL heparin, 0.1% Tween 20) and incubated for 3 hours at 65℃. Pre-hybridization solution was replaced with the mixture solution which contains digoxigenin (DIG)-labeled RNA probe and the embryos were incubated at 65℃ overnight. A series of washing steps (50% formamide/2X SSC, 2X SSC, 0.2X SSC, phosphate-buffered saline-Tween 20 [PBST]) were performed and the embryos were treated with anti-DIG-alkaline phosphatase fragment diluted 1: 1000 in blocking solution (0.5% Roche blocking reagent, 5% goat serum in PBST). After washing 15 times with PBST for 15 min, the embryos were immersed in staining solution (100 mM Tris-HCl pH 9.5, 50 mM $MgCl_2$, 100 mM NaCl, 0.1% Tween 20) three times for 10 min. Then, the embryos were colorized using nitrobuleterazolium/5-bromo, 4-chloro, 3-indolylphosphate to produce insoluble purple precipitates. Stained embryos were fixed with 4% PFA for 20 min, and dehydrated with methanol for 10 min. Then, embryos were mounted in glycerol and photographed with AxioCam ICC-1 camera on Zeiss Stemi 2000C.

15. Immunohistochemistry

Tg(sox17:egfp) embryos were fixed with 4% PFA for overnight at 4℃ and dehydrated with methanol for long storage at –20℃. Then the embryos were treated with collagenase I for 10 min at room temperature. After the collagenase I treatment, the embryos were transferred to the blocking solution (5% bovine serum albumin, 10% normal goat serum in PBST) and incubated for 3 hours at room temperature. Blocking solution was replaced with mouse anti-GFP IgG (1:200, Invitrogen) containing solution and the embryos were incubated at 4℃ overnight. A series of washing steps with PBDTT were performed and the embryos were treated with biotin-labeled goat anti-mouse IgG (1:1000, Vector Laboratories) in blocking solution for overnight at 4℃. Then, the embryos were washed with PBDTT several times and treated with AB mixture (PK-6100, Vector Laboratories) for 1 hour and transferred into 3,3'-diaminobenzidine (DAB) solution (Sigma-Aldrich). Color reaction was performed by adding 0.3% H_2O_2 into DAB solution where the embryos were immersed. Stained embryos were mounted in glycerol and photographed with AxioCam ICC-1 camera on Zeiss Stemi 2000.

16. Immunofluorescence

The embryos were fixed with 4% PFA for overnight at 4℃ and dehydrated with methanol and stored at –20℃. Then the embryos were treated with collagenase I for 10 to 45 min at room temperature depending on the developmental stages. After the collagenase I treatment, the embryos were transferred to the blocking solution (5% bovine serum albumin, 10% goat serum in PBST) and incubated for 3 hours at room temperature. Blocking

solution was replaced with primary antibody containing solution and the embryos were incubated at 4℃ overnight. Primary antibodies are anti-Cldn5 (1:50, 35-2500, Invitrogen), anti-ZO-1 (1:50, 339100, Invitrogen), anti-acetylated tubulin (1:200, T6793, Sigma-Aldrich), anti-phospho-histone H3 (1:200, 9701S, Cell Signaling) and anti-E-cadherin (1:200, 610181, BD bioscience). A series of washing steps (1% dimethyl sulfoxide [DMSO], 0.5% Triton X-100 in PBST) were performed and the embryos were treated with AF-405, 488, 546 labeled anti-mouse or rabbit IgG in blocking solution for overnight at 4℃. Then, the embryos were washed with PBDTT (1% DMSO, 0.5% Triton X-100 in PBST) for 10 times. Stained embryos were mounted in glycerol and images were obtained by Zeiss LSM700 confocal microscope with ZEN software.

17. Statistical analysis

Measurements of KV lumen area and the number and size of cilia were performed using ZEN application (Zeiss). KV lumen area was obtained by measuring the gross area in maximum intensity projection image using Closed Beizer tool of ZEN software. KV cilia size was obtained by measuring the length in maximum intensity projection image using Line tool of ZEN software. Comparisons between control and morphants were analyzed in Prism 5 (GraphPad Software, Inc.), and *P*-values were calculated by applying the unpaired two-tailed Student's *t* test

Gene	Forward primer (5' → 3')	Reverse primer (5' → 3')
cldn5a	CAAGAATTCCATGGCCTCCGCGGCTTTGGA	CAATCTAGATCACACGTAATTCCTCTTGT
cldn5b	CAAGAATTCCATGGCAAATATGATTTCTGC	CAATCTAGATCAGACGTAGTTTCGTTTAT
spaw	TGCAGCCGGTCATAGCGTGC	AGAAAACGCCGGCAGCCGAA
dand5	CGCGTTTCCCGCGTTCTTGG	TTGTCACGCGCCCTGGTTGA
cmlc1	CCCAGCCTTTTCCCATCAGCATCATG	GCGTCGGCTCACCCGGAGAG
foxj1a	ACTTCTGCTACTTCCGCCAC	GGAAGTCGGAACGGTTGGAT
lefty1	GCGCAGCACTTTTCGCGATGG	TCTCTGCCGCGTAACTGCCG

Table 1. List of primer sequences for ISH vectors.

Purpose	Gene	Forward sequence (5' → 3')	Reverse sequence (5' → 3')
PCR	***akap12α***	GCTCATGATGGAGAAACCGC	CTGGATTTCTGCTTGCACTTCC
	akap12β	ATGCTTGGGACAATAACTCTAACAG	TGAGGCCTGTCTTCTGTTGA
	cldn5a	ATGGCCTCCGCGGCTTTGGA	TCACACGTAATTCCTCTTGT
	cldn5b	ATGGCAAATATGATTTCTGC	TCAGACGTAGTTTCGTTTAT
	actb2	GCAGAAGGAGATCACATCCCTGGC	CATTGCCGTCACCTTCACCGTTC
	akap12-mutant	CCCTGAAACAATAGAAGTGCACCA	TTGTGGGCGATTCAGCTGGCA
Q-PCR	***akap12***	TGTGCAACTGCTGACAGTGA	TCCACAGACCTGTCCTCCTC
	cdh1	AGTGTGTGTGACTGCAAAGGA	GAGCAGAAGAAGAGCAAGCAA
	actb2	CATCCATCGTCCACCGCAAA	CCTGAGTCAAGCGCCAAAAA
	dand5	GCCGTTAGTCATGTGCCGTT	CTATGGGTCAGGATTGCGGG
	eef1a1l1	CTGGAGGCCAGCTCAAACAT	ATCAAGAAGAGTAGTACCGCTAGCATTAC
	akap12-mutant	GGAAGCAGAGAGTGGTGCTG	TCCTCTGCTGCAGGTTCCTC

Table 2. List of primer sequences for PCR and Q-PCR

Purpose	Primer name	Primer sequence (5' → 3')
Targeting Tol2 to BAC	pTarBAC_HA1_iTol2_F	gcgtaagcggggcacatttcattacctctttct ccgcacccgacatagatCCCTGCTCGAGCCGGG CCCAAGTG
	pTarBAC_HA2_iTol2_R	gcggggcatgactattggcgcgccggatcgatc cttaattaagtctactaATTATGATCCTCTAGA TCAGATC
Tol2 confirmation	pTarBAC_HA1_control_R	CTGTCAAACATGAGAATTGGTC
	amp_HA1_control_R	ACATTTCCCCGAAAAGTGG
	amp_HA2_control_F	CTGAGATAGGTGCCTCACTG
	pTarBAC_HA2_control_R	GAGAGCCTTCAACCCAGTC
Targeting XFP to *akap12β* region of BAC	*akap12β*_HA1_GFP_F	acggcaaatctttttttttttttctctgagaag tgtttgcaaaagtttttACCATGGTGAGCAAGG GCGAGGAG
	*akap12β*_HA2_kanR_R	caattcatagatttaaaatgcatcttacctgtt agagttattgtcccaagTCAGAAGAACTCGTCA AGAAGGCG
XFP confirmation	*akap12β*_HA1_control-F	CACCCAGAAACCGAGAAGAA
	*akap12β*_HA1_control-R	AAAAACCCACTAACCATCTCCA

Table 3. List of primer sequences for BAC modification.

RESULTS

1. *akap12β* is the major isoform of *akap12* during KV development.

First, the spatiotemporal expression of *akap12* was examined by *in situ* hybridization (ISH). *akap12* was highly expressed in mesodermal cell as previously reported. However, the expression of *akap12* is not exclusive in mesodermal cells (Fig. 6A, 6B). *akap12* was expressed in *sox17*-positve DFCs which is the progenitors of KV and derived from non-involuting endocytic marginal cell (Fig. 6A', 6B'). Two color ISH of *akap12* with *dand5,* the marker for the KV, revealed that the expression of *akap12* was not detected at 6 ss when the leftward nodal signal is initiated from the mature KV (Fig. 6C). Thus, the expression of *akap12* was transiently detected in KV lineage cells when the cluster of DFC undergo collectively migration. In zebrafish, two isoforms of *akap12, akap12α and akap12β,* were identified. Each isoform has distinct promoter region and shows different expression pattern during embryo development (Fig. 7A, 7B). The expression of *akap12α* was initiated from bud stage, and that of *akap12β* was initiated from sphere stage. Interestingly, the expression of *akap12* at 75% epiboly stage was significantly reduced by *akap12β* MO injection, while *akap12α* MO injection was ineffective to reduce *akap12* expression (Fig. 7C, 7D). Thus, I demonstrated that *akap12β* is the major isoform of *akap12* during KV development.

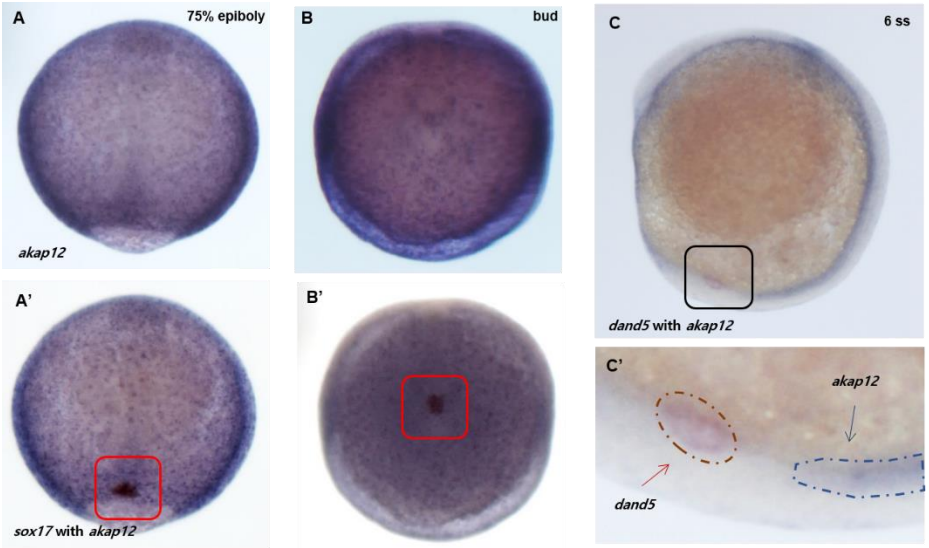

Figure 6. *akap12* expression in KV lineage cells.

(A, A') Expression of *akap12* within *sox17*-positve DFCs at 75% epiboly was marked by a red rectangle. **(B, B')** Expression of *akap12* within *sox17*-positve DFCs at bud stage was marked by a red rectangle. **(C, C')** Expression of *akap12* and *dand5* at 6 ss.

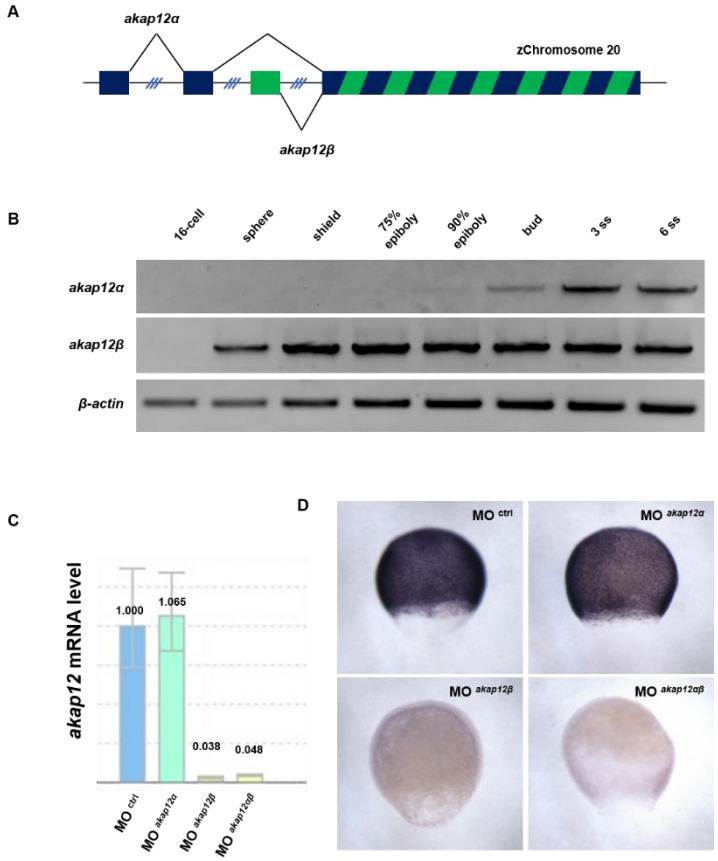

Figure 7. *akap12β* is the major isoform of *akap12* during gastrula period.

(A) Genomic locus of *akap12* in zebrafish. **(B)** RT-PCR analysis of two *akap12* isoforms. **(C)** qRT-PCR analysis of *akap12* mRNA at 75% epiboly stage in control, *akap12α, akap12β* and *akap12α&β* morphants. **(D)** *In situ* hybridization image of *akap12* at 75% epiboly stage in control, *akap12α, akap12β* and *akap12α&β* morphants.

2. Organ laterality was disrupted in *akap12β* morphants.

Specific expression of *akap12β* in KV lineage cells suggests that *akap12β* might influence asymmetric organ development by modulating KV formation in zebrafish. Thus, the status of the heart, a representative asymmetric organ, was investigated by *in situ* hybridization of *cmlc1* in *akap12β* morphants. *akap12β* morphants exhibited the middle (20%) and reversed (12%) heart, while only 1% of the control morphants showed the heart laterality defects (Fig. 8). To validate whether the disrupted heart laterality in *akap12β* morphants might result from abnormal KV, I performed *in situ* hybridization of *spaw*, the *nodal*-related gene, which propagates through the left lateral plate mesoderm from KV and determines laterality of the organs. *akap12β* morphants exhibited bilateral (19%) and right-sided (13%) *spaw* expression, while 6% of the control morphants showed bilateral *spaw* expression (Fig. 9). In addition, I performed *in situ* hybridization of *lefty1*, the midline molecular barrier, which is expressed in notochord and restricts nodal activity to the left lateral plate mesoderm. Both control and *akap12β* morphants showed normal expression of *lefty1* in notochord, regardless of dorsal curvature (Fig. 10). Finally, the expression of *dand5*, which is expressed around the KV and acts as a molecular barrier of *spaw,* was investigated. Expression patterns of *dand5* in control morphants were mostly normal with a horseshoe shape, however, 58% of *akap12β* morphants showed abnormal *dand5* expression (Fig. 11). These data substantiated that *akap12β* downregulation results in disruption of asymmetric signals and organ laterality.

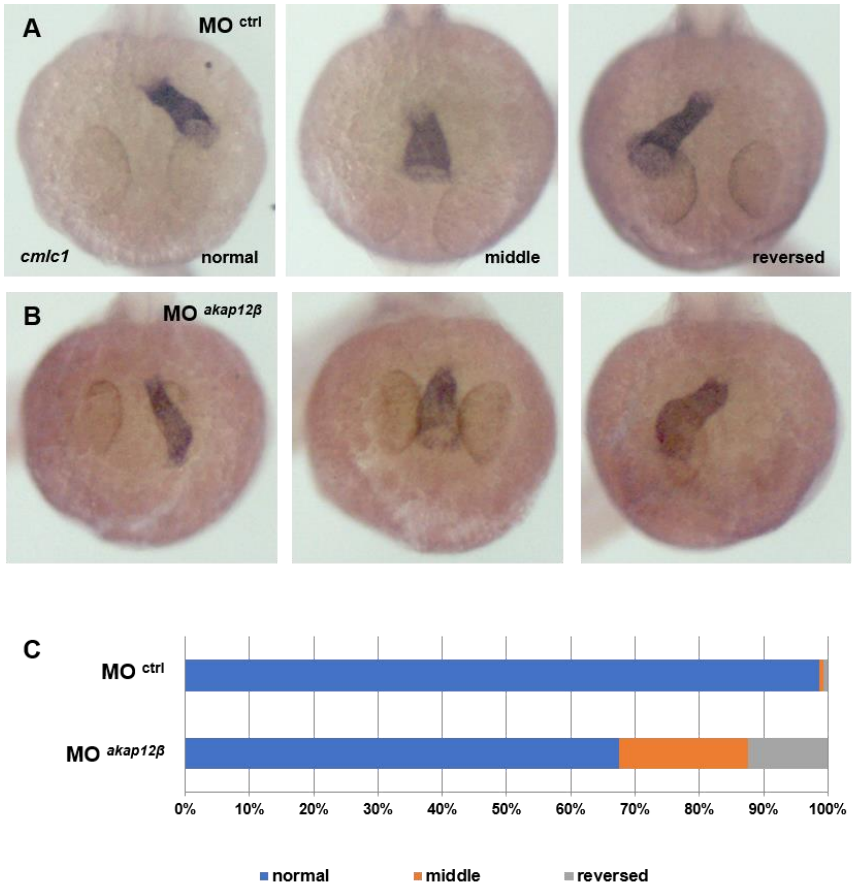

Figure 8. Heart laterality was disrupted in *akap12β* morphants.

(A, B) Visualization of heart by i*n situ* hybridization of *cmlc1* in 30 hpf embryos. Representative images of control morphants (A), *akap12β* morphants (B). **(C)** Statistical stacked bar graph (blue; normal, orange; middle, grey; reversed, control morphants; n = 154, *akap12β* morphants; n = 143).

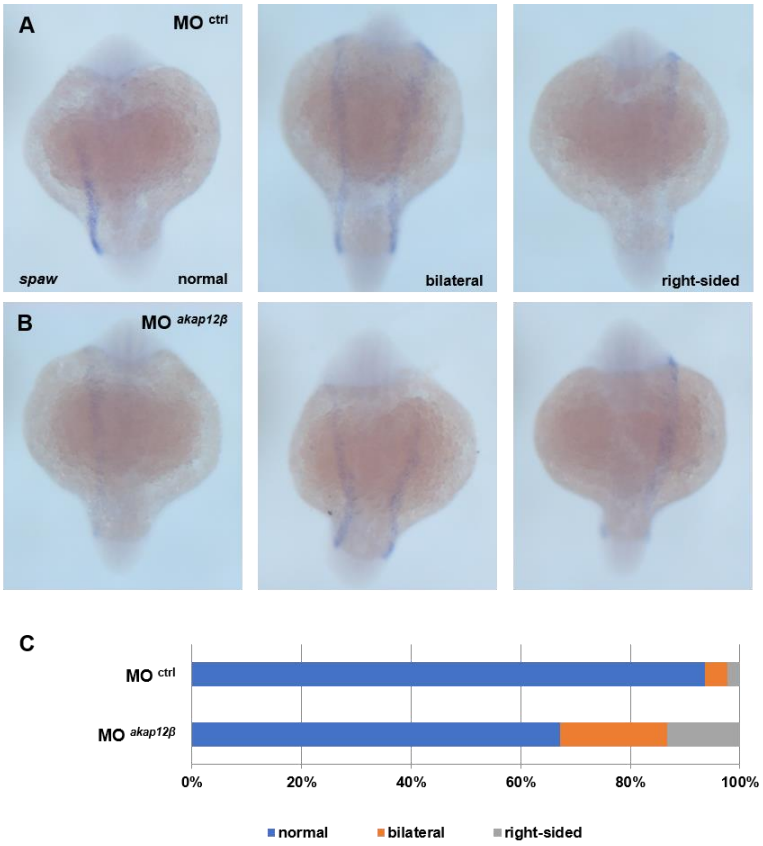

Figure 9. Expression of *spaw* was disrupted in DFC *akap12β* morphants.

(A, B) Visualization of *spaw* by *in situ* hybridization in 18 ss embryos. Representative images of control morphants (A) and *akap12β* morphants (B). **(C)** Statistical stacked bar graph (blue; normal, orange; bilateral, grey; right-sided, control morphants; n = 174, *akap12β* morphants; n = 195).

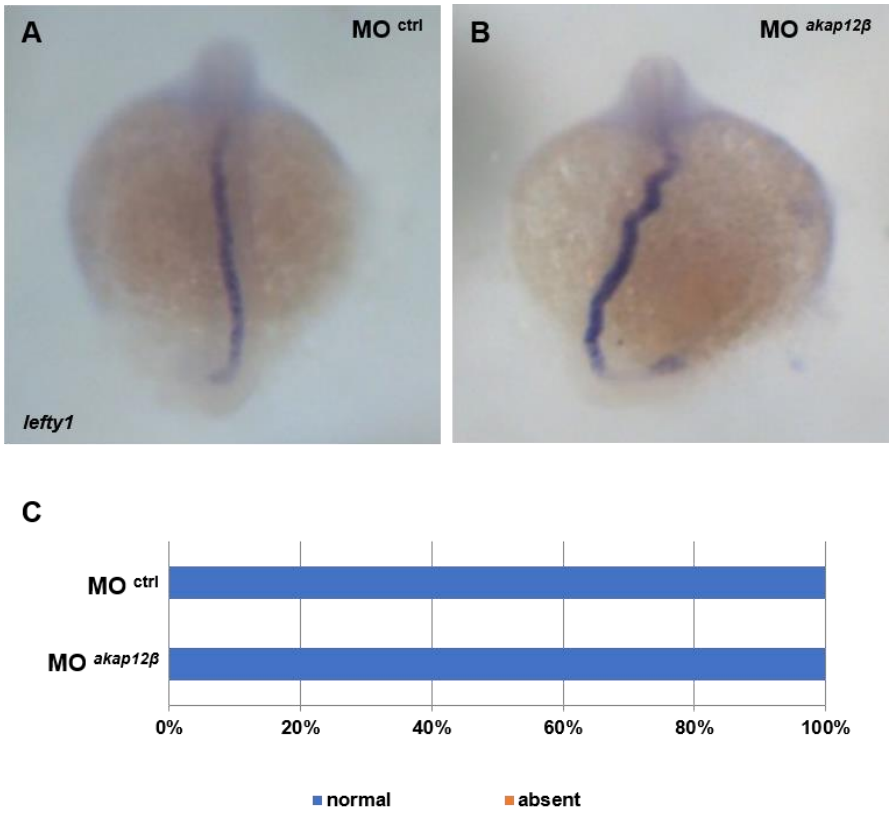

Figure 10. Expression of *lefty1* was normal in *akap12β* morphants.

(A, B) Visualization of *lefty1* by *in situ* hybridization in 18 ss embryos. Representative images of control morphants (A) and *akap12β* morphants (B). **(C)** Statistical stacked bar graph (blue; normal, orange; absent, control morphants; n = 74, *akap12β* morphants; n = 92).

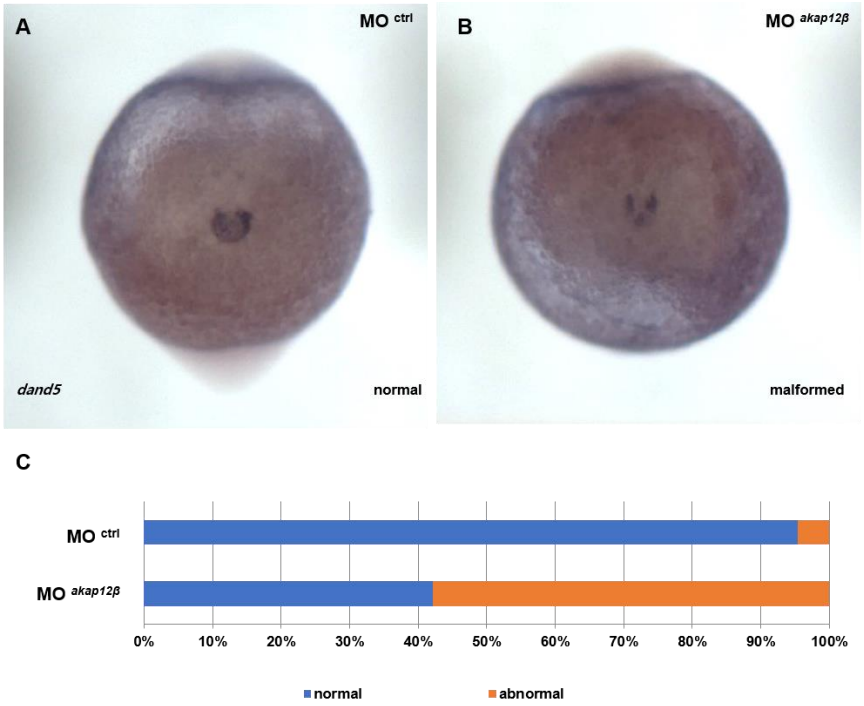

Figure 11. Expression of *dand5* was disrupted in *akap12β* morphants.

(A, B) Visualization of *dand5* by *in situ* hybridization in 6 ss embryos. Representative images of control morphants (A) and *akap12β* morphants (B). **(C)** Statistical stacked bar graph (blue; normal, orange; malformed, control morphants; n = 86, *akap12β* morphants; n = 110).

3. Organ laterality defects were also exhibited in DFC *akap12β* morphants.

To ensure that the disrupted organ laterality in *akap12β* morphants resulted from downregulation of *akap12β* in KV lineage cells, I injected the *akap12β* MO into yolk at 128 to 512-cell stage for exclusive reduction of *akap12β* in KV lineage cells. Since the marginal blastomeres are connected to the yolk cell by cytoplasmic bridge, DFC-specific injected MO is restricted in the boundary between the blastomeres and yolk where the KV lineage cells exist (Fig. 12). DFC-specific *akap12β* morphants showed disrupted heart laterality (41%) and aberrant *spaw* expression (25%), whereas DFC control morphants showed a low rate of these defects (Fig. 13).

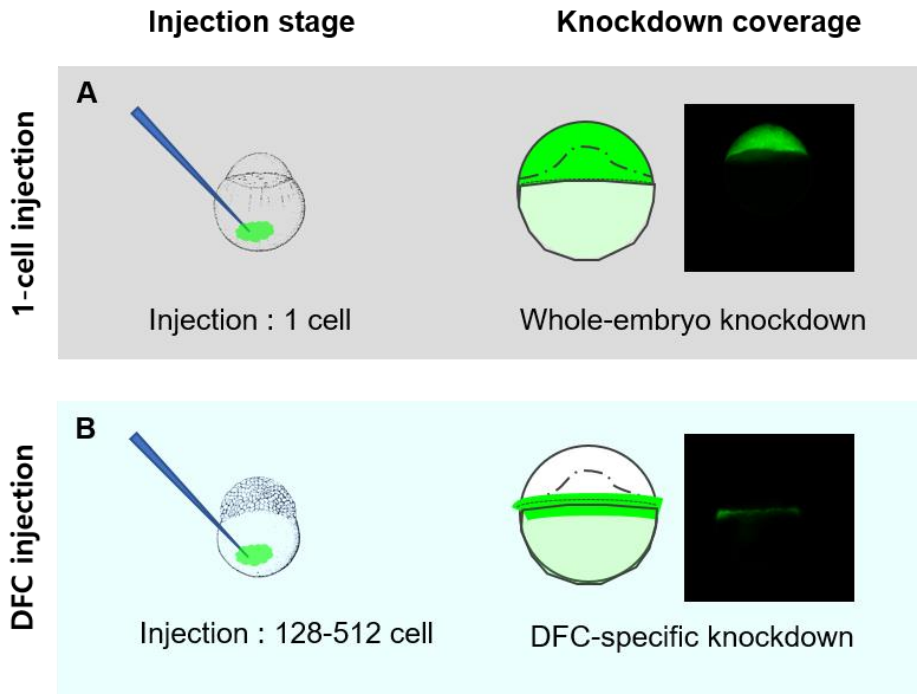

Figure 12. DFC-specific MO injection method.

(A) Illustration of 1-cell MO injection method and its knockdown coverage. **(B)** Illustration of DFC-specific injection method and its knockdown coverage.

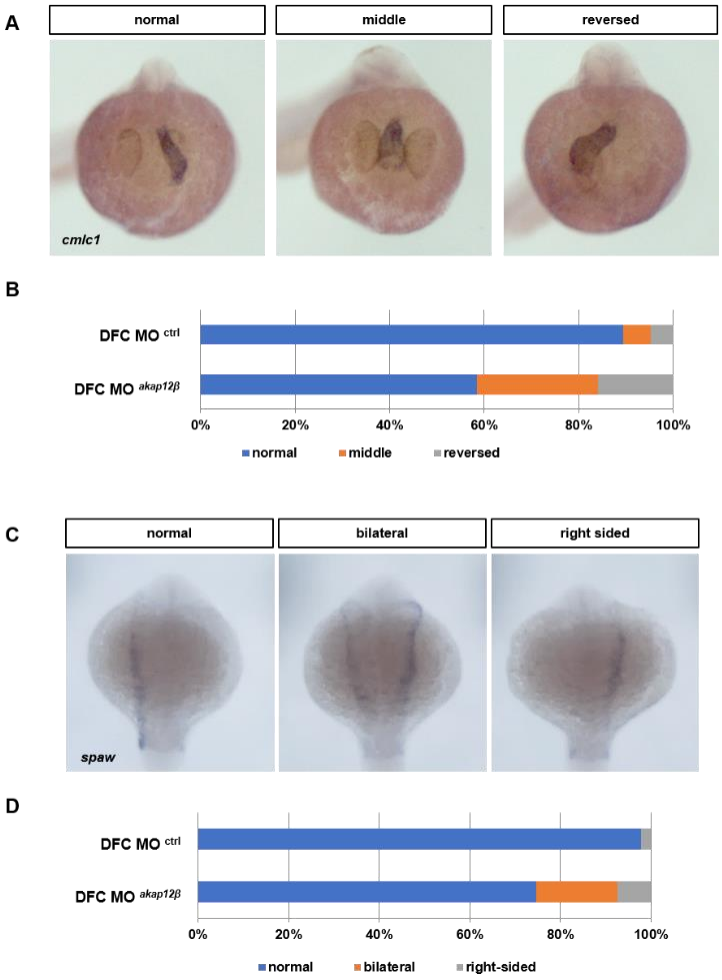

Figure 13. Left-right asymmetry was disrupted in DFC *akap12β* morphants.

(A) Representative images of normal, middle and reversed heart laterality. **(C)** Statistical stacked bar graph (Blue; normal, Orange; middle, grey; reversed, DFC control morphants; n = 85, DFC *akap12β* morphants; n = 94). **(C)** Representative images of normal, bilateral and right-sided *spaw* expression. **(C)** Statistical stacked bar graph (blue; normal, orange; bilateral, grey; right-sided, DFC control morphants; n = 45, DFC *akap12β* morphants; n = 67).

4. KV was malformed in DFC *akap12β* morphants.

I demonstrated that the disrupted organ laterality was derived from a deficiency of *akap12β* in KV lineage cells. Thus, the morphology of KV was examined in DFC *akap12β* morphants. Differential interference contrast (DIC) images of living embryos showed that the size of KV in DFC *akap12β* morphants was relatively smaller than the that of DFC control morphants (Fig. 14A, 14B). To compare the exact size of KV, KV apical lumen was visualized by immunostaining of Cldn5 (Fig. 14C, 14D). DFC *akap12β* morphants showed decreased lumen area (3704 ± 463.5 μm^2), compared with DFC control morphants (5913 ± 661.4 μm^2) (Fig. 14E). Then, I visualized the motile monocilia within KV by immunostaining of acetylated tubulin (Fig. 15A, 15B). The number of cilia was 50.75 ± 4.47 and 36.06 ± 4.47 per embryos in DFC control and DFC *akap12β* morphants, respectively (Fig. 15C). Since the size of KV lumen and the number of cilia were decreased in DFC *akap12β* morphants, I calculated the KV lumen area for each cilium. XY point graph showed that the relativity between the number of cilia and the KV lumen area in DFC control and DFC *akap12β* morphants (Fig. 16A-16C). Interestingly, the KV lumen area for each cilium in DFC *akap12β* morphants (111.7 ± 7.45 μm^2) was comparable to that in DFC control morphants (118.0 ± 7.80 μm^2). These data suggest that the decreased KV lumen size might result from the decreased number of KV epithelial cells.

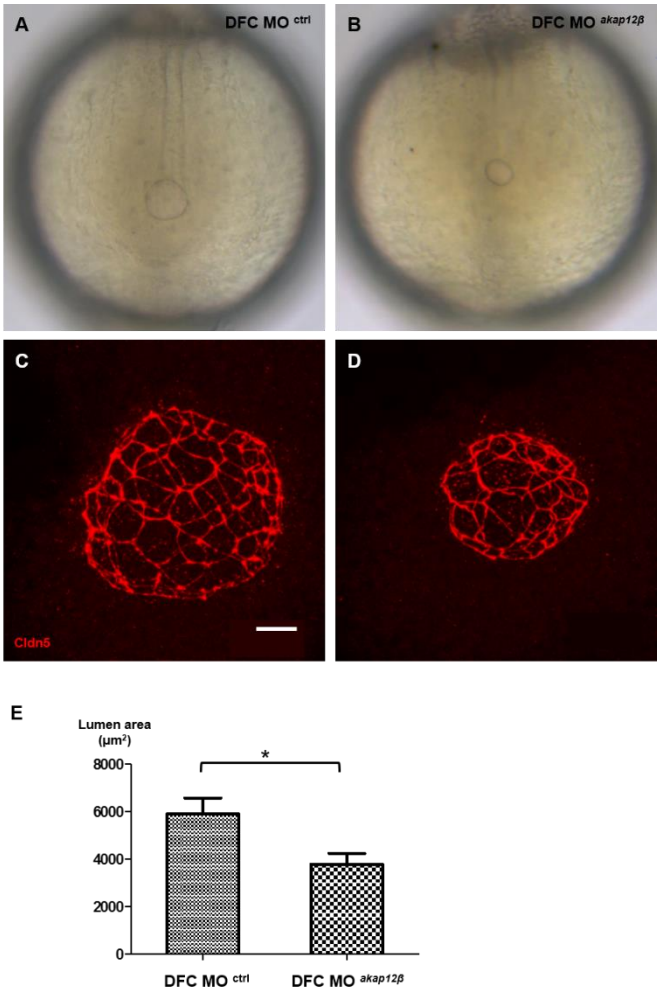

Figure 14. KV lumen size was decreased in DFC *akap12β* morphants.

(A, B) Representative images of DFC control morphants (A) and DFC *akap12β* morphants (B). **(C, D)** Visualization of KV lumen by immunolabeling of Cldn5 in 6 ss embryos. Representative images of DFC control morphants (C) and DFC *akap12β* morphants (D). **(E)** Statistical column bar graph (DFC control morphants; n = 10, DFC *akap12β* morphants; n = 13). scale bar: 20μm

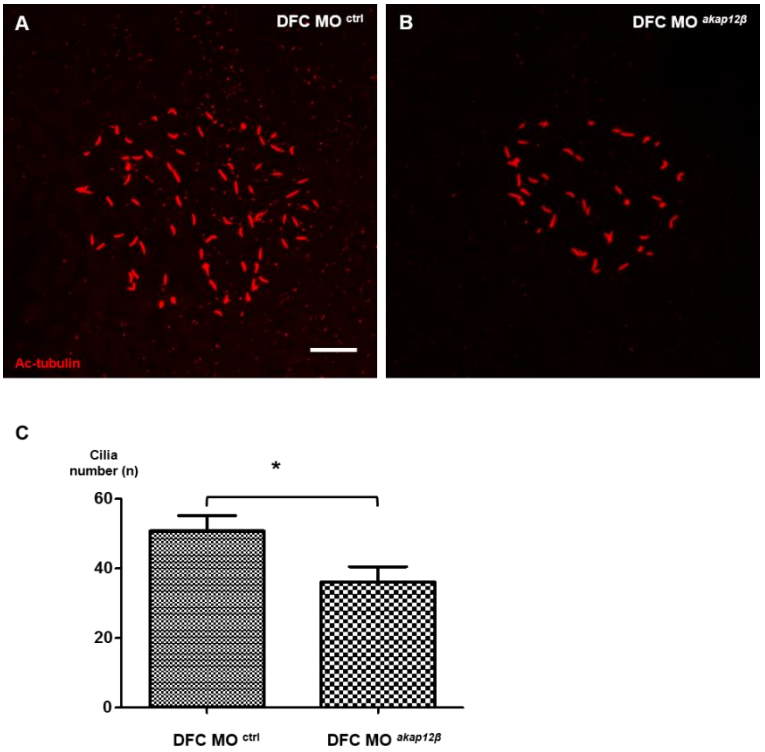

Figure 15. The number of cilia was decreased in DFC *akap12β* morphants. **(A, B)** Visualization of KV cilia by immunolabeling of acetylated tubulin in 6 ss embryos. Representative images of DFC control morphants (A) and DFC *akap12β* morphants (B). **(C)** Statistical column bar graph (DFC control morphants; n = 16, DFC *akap12β* morphants; n = 17). scale bar: 20μm

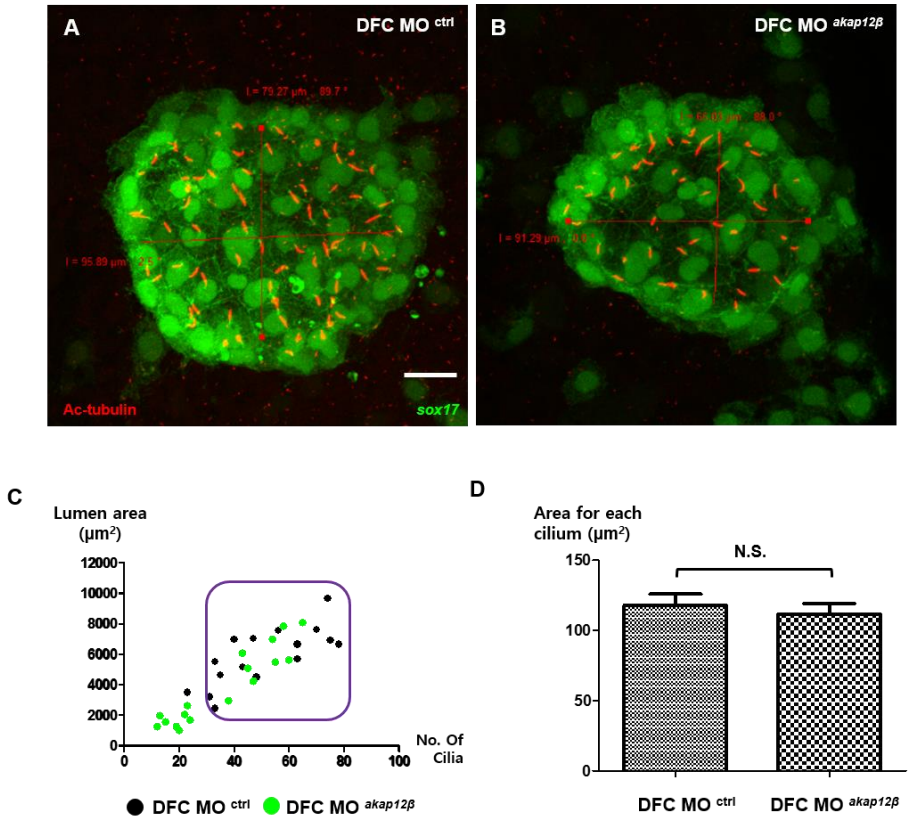

Figure 16. The area for each cilium in DFC *akap12β* morphants.

(A, B) Visualization of KV cilia by immunolabeling of acetylated tubulin in 6 ss embryos. Representative images of DFC control morphants (A) and DFC *akap12β* morphants (B). **(C)** Statistical XY point graph (DFC control morphants; n = 16, DFC *akap12β* morphants; n = 17). **(D)** Statistical column bar graph (DFC control morphants; n = 15, DFC *akap12β* morphants; n = 9). scale bar: 20μm

5. The cluster of DFC was fragmented in DFC *akap12β* morphants.

Since the number of monocilia was decreased in DFC *akap12β* morphants, I examined the proliferation rate of progenitor cells by immunostaining of phospho-histone H3 (pH3) at 75% epiboly. The number of pH3-positive DFCs in DFC *akap12β* morphants (2.083 ± 0.468) was comparable to that of DFC control morphants (1.875 ± 0.480) (Fig. 17). However, the cluster of DFC was fragmented in DFC *akap12β* morphants (Fig. 17B). To statistically examined the DFC fragmentation ratio, DFCs were visualized by immunostaining of *sox17*-promoter induced EGFP at 75% epiboly. It was shown that the 30% of DFC *akap12β* morphants exhibited the fragmentation of *sox17*-positive DFC cluster, while only 1% of DFC control morphants exhibited DFC fragmentation (Fig.18A-18C). To clarify the DFC fragmentation phenotype in DFC *akap12β* morphants, the DFCs were visualized by *in situ* hybridization of *foxj1a* at 75% epibloy. DFC *akap12β* morphants showed the fragmentation of *foxj1a*-positive DFC cluster (39%), while DFC control morphants showed a single DFC cluster without fragmentation (Fig. 18D-18F). This broken-up DFC cluster is the representative phenotype of a failure of cell collectivity. Cell collectivity within DFCs is maintained by cadherin-1 based adherence junction. Thus, the Cdh1 was visualized by immunostaining at 75% epiboly. Cdh1 was highly expressed at intercellular spaces between DFCs in DFC control morphants (Fig. 19A). However, the expression of Cdh1 within DFCs was significantly reduced in DFC *akap12β* morphants (Fig. 19B). Furthermore, not only the protein expression but also the mRNA expression level was decreased in *akap12β* morphants (Fig. 19C). These data elucidate that the malformed KV in DFC *akap12β* morphants resulted from DFC fragmentation by downregulation of

Cdh1. Finally, *GFP-akap12β* mRNA was injected with MOs to rescue *akap12β* morphants phenotypes. Fragmentation of DFC cluster was rescued by *GFP-akap12β*. *akap12β* morphants with *GFP-akap12β* showed a higher rate of normally formed DFC cluster without fragmentation (76%) than that in *akap12β* morphants (57%) (Fig. 20A-20D). Furthermore, the KV lumen area was restored in *akap12β* morphants with *GFP-akap12β* (3309 ± 365.5 μm^2), compared with that in *akap12β* morphants (1887 ± 288.7 μm^2). These data suggest that the laterality defects in *akap12β* morphants resulted from the loss of cell collectivity within KV lineage cells.

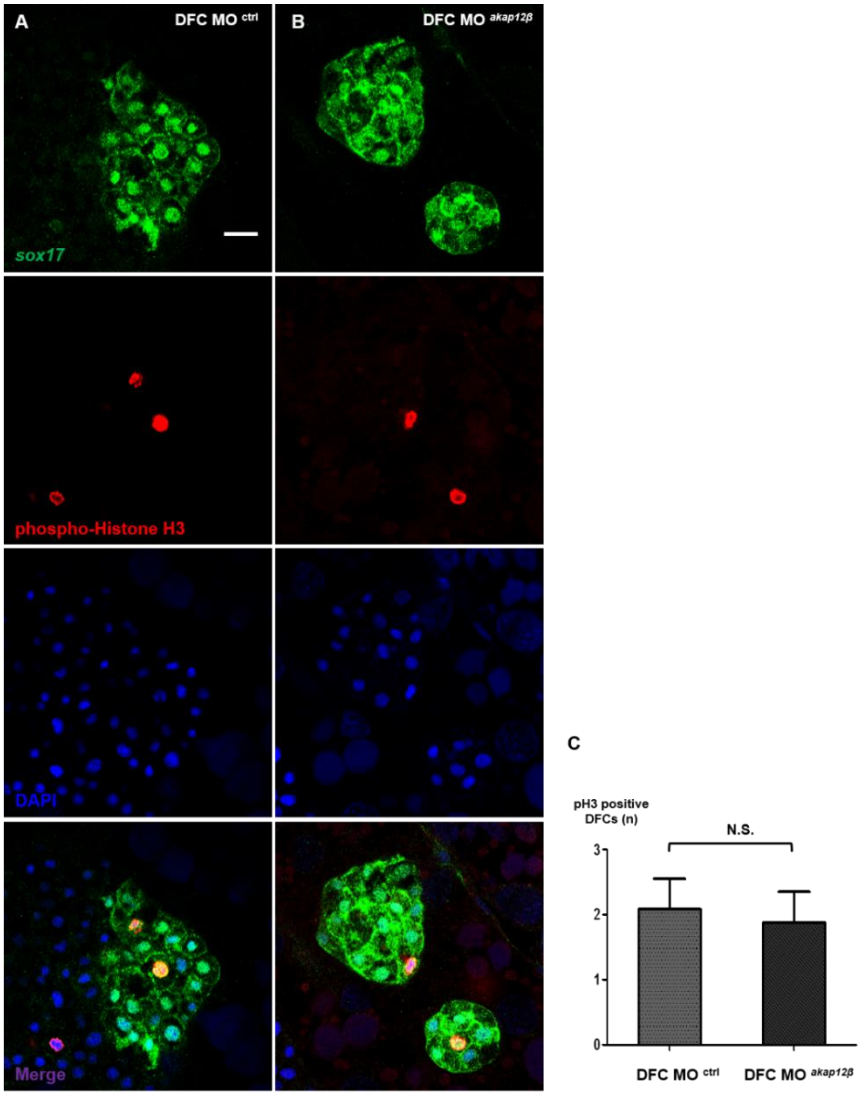

Figure 17. The number of proliferative DFCs in DFC *akap12β* morphants. **(A, B)** Visualization of proliferatvie cells by immunolabeling of phospho-Histone H3 in 75% epiboly embryos. Representative images of DFC control morphants (A) and DFC *akap12β* morphants (B). **(C)** Statistical column bar graph (DFC control morphants; n = 12, DFC *akap12β* morphants; n = 8). scale bar: 20μm

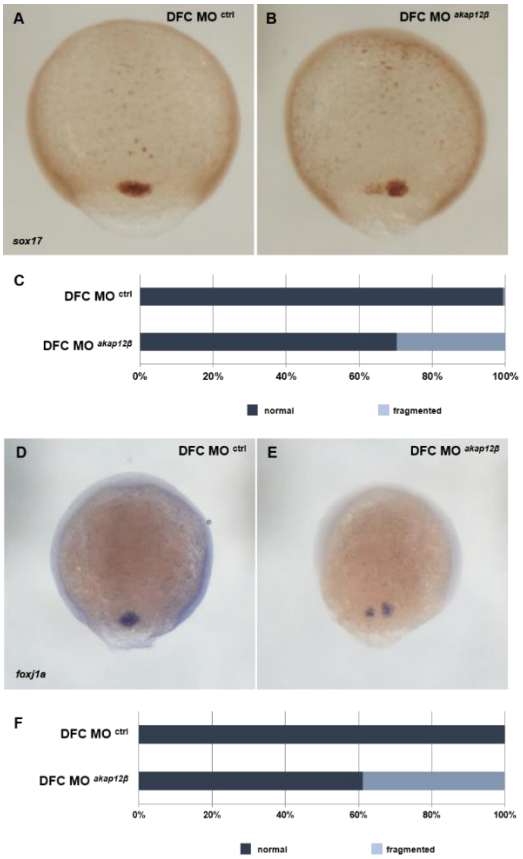

Figure 18. The cluster of DFCs was fragmented in DFC *akap12β* morphants.

(A, B) Visualization of DFCs by immunostaining of *sox17*-promoter induced EGFP in 75% epiboly embryos. Representative images of DFC control morphants (A) and DFC *akap12β* morphants (B). **(C)** Statistical stacked bar graph (DFC control morphants; n = 82, DFC *akap12β* morphants; n = 77). **(D, E)** Visualization of DFCs by *in situ* hybridization of *foxj1a* in 75% epiboly embryos. Representative images of DFC control morphants (A) and DFC *akap12β* morphants (B). **(F)** Statistical stacked bar graph (DFC control morphants; n = 22, DFC *akap12β* morphants; n = 36).

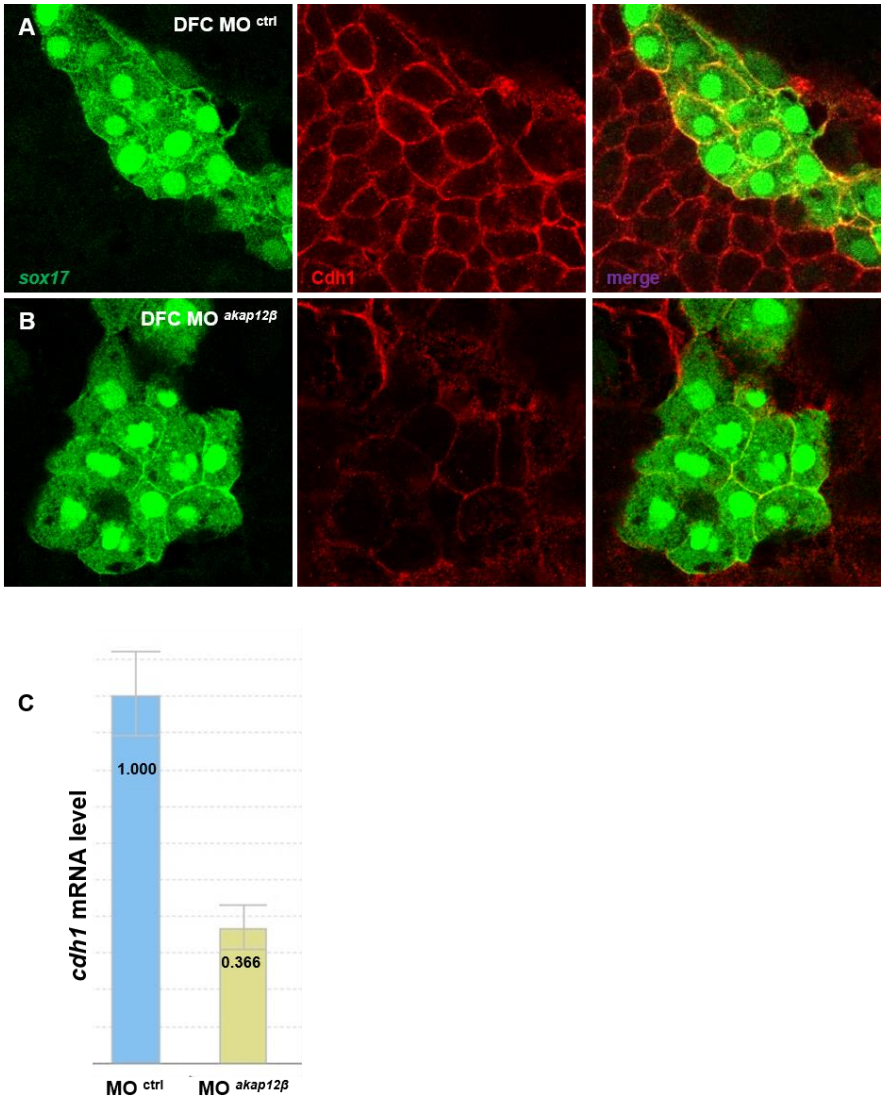

Figure 19. Cdh1 was suppressed in *akap12β* morphants.

(A, B) Visualization of Cdh1 with *sox17*-promoter induced EGFP in 75% epiboly embryos. Representative images of DFC control morphants (A) and DFC *akap12β* morphants (B). **(C)** qRT-PCR analysis of *cdh1* mRNA in control and *akap12β* morphants.

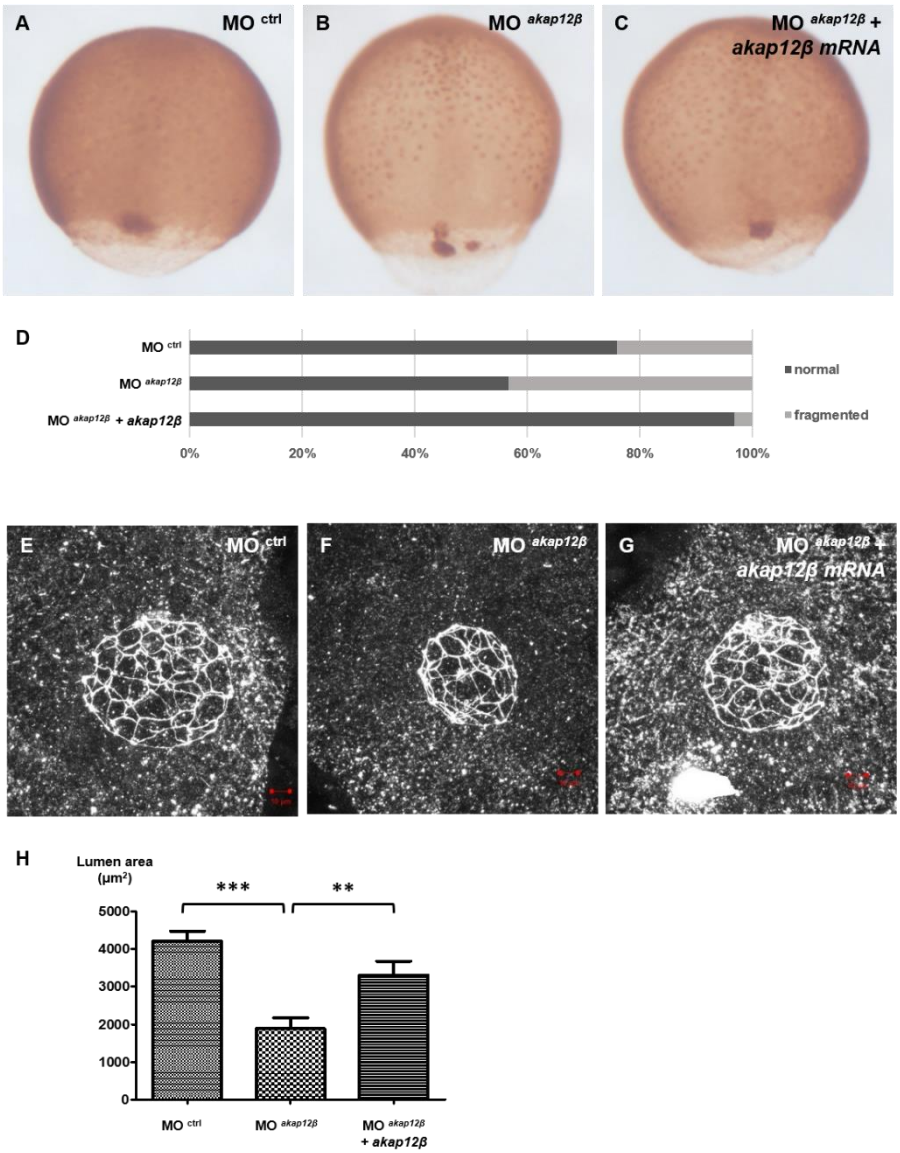

Figure 20. Defective phenotypes of *akap12β* morphants were restored by exogenous *akap12β* mRNA.

(A–C) Visualization of DFCs by immunostaining of *sox17*-promoter induced EGFP in 75% epiboly embryos. Representative images of control morphants

(A), *akap12β* morphants (B) and *akap12β* morphants with *akap12β* mRNA (C). **(D)** Statistical stacked bar graph (dark-grey; normal, grey; fragmented, control morphants; n = 32, *akap12β* morphants; n = 30, *akap12β* morphants with *akap12β* mRNA; n = 35). **(E–G)** Visualization of KV lumen by immunolabeling of Cldn5 in 6 ss embryos. Representative images of control morphants (A), *akap12β* morphants (B) and *akap12β* morphants with *akap12β* mRNA (C). **(H)** Statistical column bar graph (control morphants; n = 10, *akap12β* morphants; n = 10, *akap12β* morphants with *akap12β* mRNA; n = 11). *** depicts $p<0.001$, ** depicts $p<0.01$, error bars indicates s.e.m., scale bar: 20μm

6. Generation of TALEN-mediated *akap12* mutant.

Transcription activator-like effector nuclease (TALEN) is the 2nd generation of engineered nuclease and capable of editing specific genome sequences in living organisms. TALEN is consist of specific-DNA sequence binding module protein and non-specific restriction endonuclease FokI. Specific TALEN pair targeting coding sequence (CDS) region of *akap12* was generated and injected into zebrafish embryos with the help of Toolgene.inc (Fig. 21). Then, the grown F0 zebrafish was mated with WT zebrafish. To identify *akap12* mutant embryos, 3 types of analysis were performed including T7E1 assay, enzyme restriction of deletion site and melting temperature analysis. First, genomic DNA was isolated by tail fin amputation of adult zebrafish and amplified by PCR. Since the T7E1 enzyeme cleaves mismatch point of heteroduplex DNA, amplicons were melt and reannealed. Then, the amplicon of heteozygous *akap12* mutant was cleaved by T7E1 (Fig. 22A). Identified *akap12* mutant amplicon was cloned into pGemT-easy vector and sequenced (Fig. 22B). Next, *akap12* mutant and WT sibling were distingished by AlwNI enzyme assay. Though the T7E1 assay cleaves heteroduplex DNA, regardless of nucleotide sequnce information, both WT and homozygous mutant remain uncleaved. Thus, the AlwNI restriction enzyme, which specifically cleaves WT amplicon, was incubated with WT, heterozygous, and homozygous *akap12* mutant amplicon to distinguish them respectively (Fig. 23). Finally, melting temperature analysis was conducted to confirm *akap12* mutant. The principle of melting temerature analysis is that flurorescent dye containg amplicon releases its intercalating dye by gradual temperature increase and monitoring the dye release in real-time enables the distinguishment of WT and mutant. The melt curve images derived

from the reporter release showed the Tm value difference between the WT, heterozygous *akap12* mutant and homozygous *akap12* mutant amplicon. The Tm values were 77.83 in WT sibling, 77.23 in heterozygous *akap12* mutant, and 75 in homozygous *akap12* mutant amplicon, respectively (Fig. 24). Thus, the *akap12* mutant was identified by upper 3 types of analysis.

The organ laterality in *akap12* mutant and WT sibling was investigated by *in situ* hybridization of *cmlc1*. It was shown that the 6% of *akap12β* mutant exhibited the disrupted heart laterality, while 1% of WT sibling exhibited the disrupted heart laterality (Fig. 25). However, offspring from heterozygous *akap12* mutant showed a little higher rate of heart laterality defects (7%) than *akap12* mutant. It needs further elucidation whether the role of *akap12* in left-right asymmetric development was compensated in homozygous *akap12* mutant during mutagenesis.

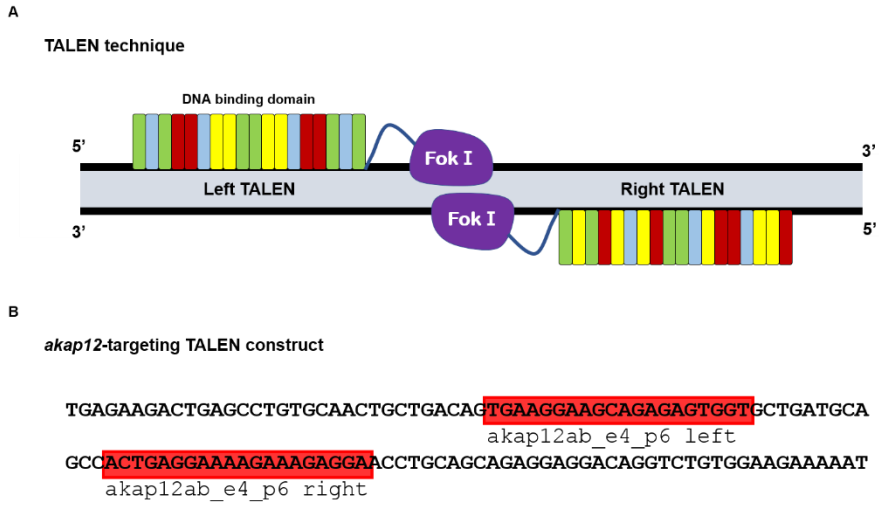

Figure 21. TALEN-mediated *akap12* mutagenesis.

(A) Illustration of site-directed mutagenesis by TALEN method. **(B)** Specific TALEN pair targeting *akap12* CDS region.

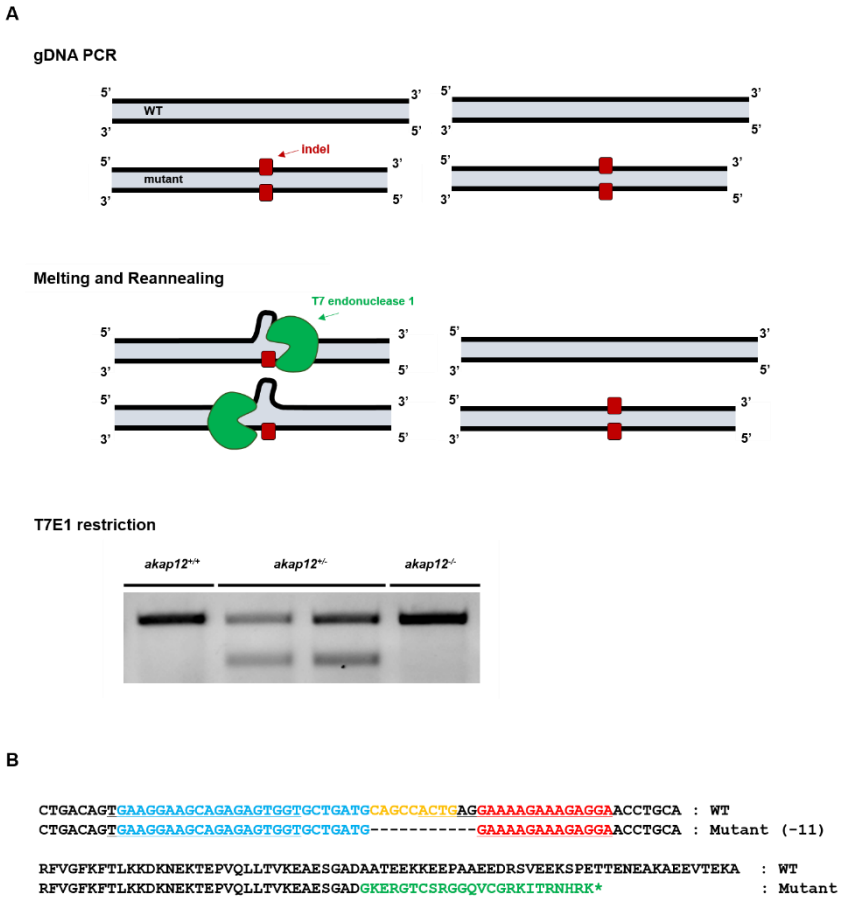

Figure 22. T7E1 analysis to identify *akap12* mutant embryos.

(A) Illustration of T7E1 analysis. **(B)** Nucleotide and amino acid sequences of constructed *akap12* mutant zebrafish.

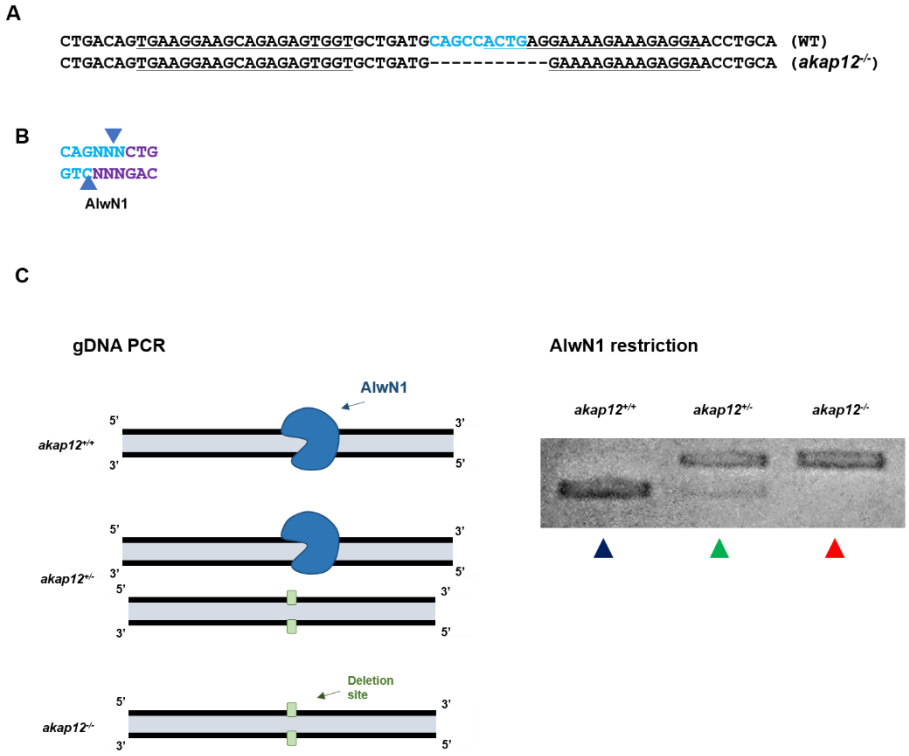

Figure 23. AlwN1 restriction analysis to confirm *akap12* mutant embryos. **(A)** Nucleotide sequence of constructed *akap12* mutant zebrafish. **(B)** AlwN1 enzyme restriction site. **(C)** *akap12* mutant and WT sibling gDNA treated with AlwN1 restriction enzyme.

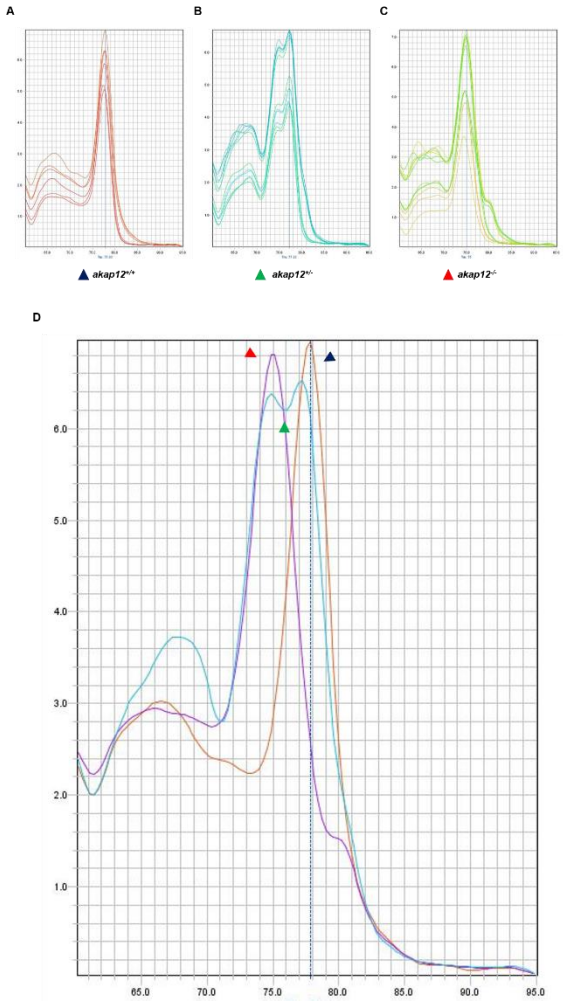

Figure 24. Melting temperature analysis to confirm *akap12* mutant embryos.

(A-C) Melting temperature curve images of WT sibling marked by a blue arrow (A), *akap12*$^{+/-}$ mutant marked by a green arrow (B) and *akap12*$^{-/-}$ mutant embryos marked by a red arrow (C). **(D)** Summarized images of WT sibling, *akap12*$^{+/-}$ and *akap12*$^{-/-}$ mutant embryos.

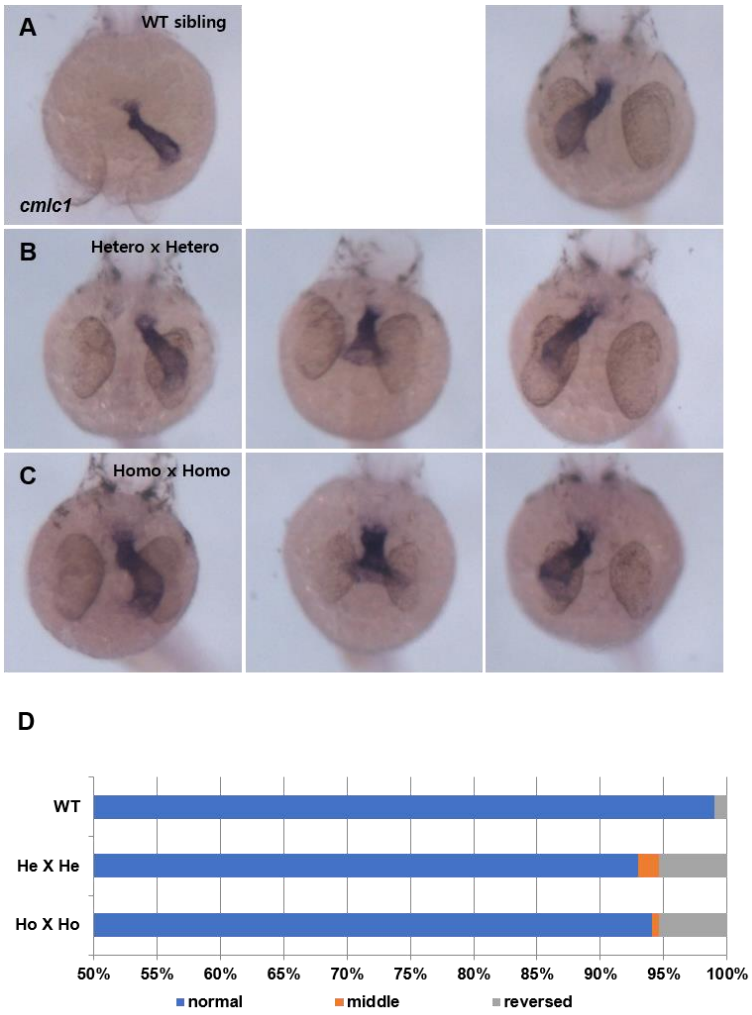

Figure 25. Laterality of heart in *akap12* mutant embryos.

(A-C) Visualization of heart by i*n situ* hybridization of *cmlc1* in 30 hpf embryos. Representative images of WT sibling (A), *akap12*$^{+/-}$ mutant (B) and *akap12*$^{-/-}$ mutant embryos (C). **(D)** Statistical stacked bar graph (blue; normal, orange; middle, grey; reversed, WT sibling; n = 99, *akap12*$^{+/-}$ mutant embryos; n = 185, *akap12*$^{-/-}$ mutant embryos; n = 186).

7. Construction of *Tg(akap12β:mCheery-caax)* by BAC modification

To ascertain the specific expression of *akap12β* in zebrafish, *Tg(akap12β:mCheery-caax)* was constructed through the modified bacterial artificial chromosome (BAC) vector injection. Detailed protocol of BAC modification followed the preceding article with minor modification. First, BAC vector (Ch73-192G21), which contains the *akap12β* promoter region, was purchased from BACPAC resources center (Fig. 26). Since the BAC was preserved in homology directed repair (HDR)-deficient E.Coli to reduce the possibility of mutation, HDR-gene containing vector, pRedET, was transfected into the E.Coli (Fig. 27A, B). Then, the BAC targeting tol2 sequence amplicon was transfected into the E.Coli to modify the BAC vector to have transposon element (Fig. 27C). Next, *akap12β* ATG region targeting *mCheery-caax* sequence amplicon was transfected into E.Coli to make the *mCherry-caax* be transcribed instead of *akap12β* under *akap12β* promoter (Fig. 27D). Modified BAC*(akap12β:mCheery-caax)* vector was isolated and injected with transposase into 1-cell embryo (Fig. 27E, F). Embryo injected with BAC*(akap12β:mCheery-caax)* showed the partial expression of mCherry at heart, somatic muscle and circulating blood cells at 30 hpf (Fig. 28).

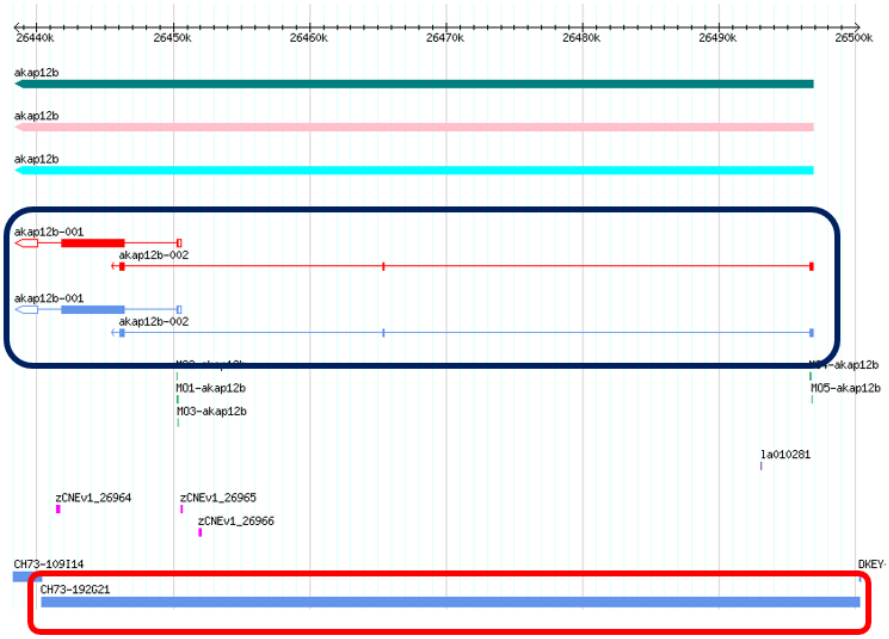

Figure 26. BAC vector containing *akap12β* promoter region.

Identification of *akap12β* promoter region containing BAC vector, CH73-192G21.

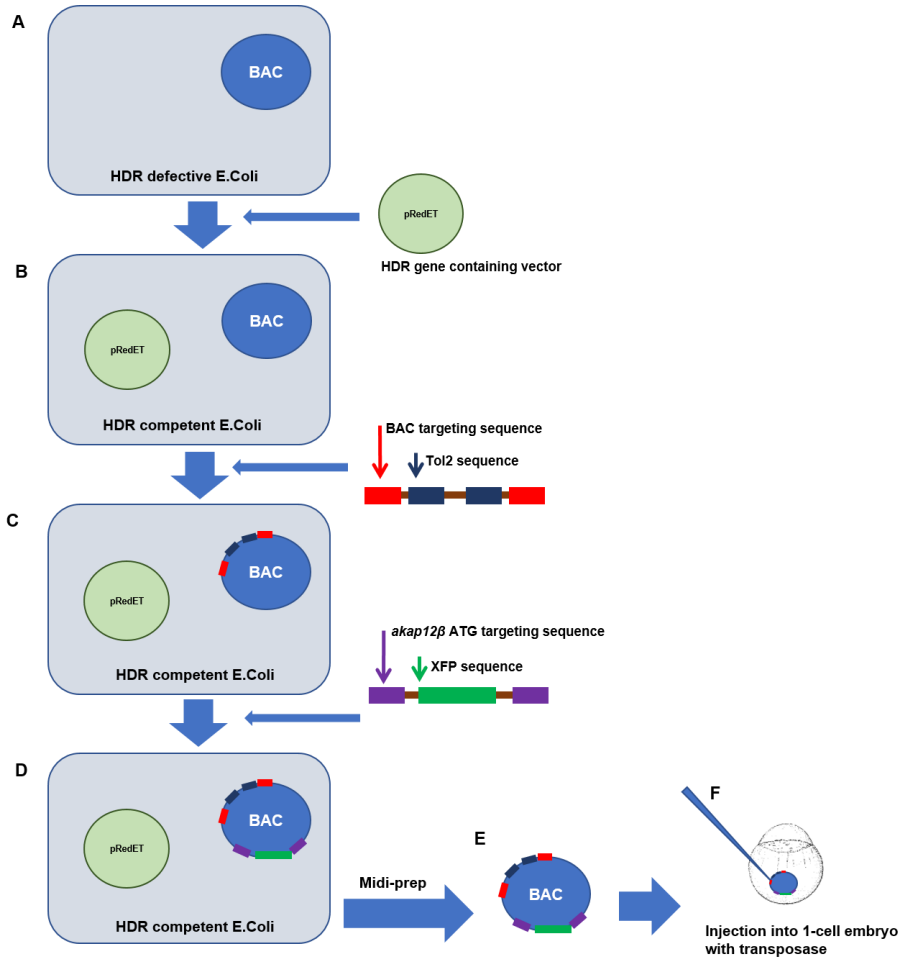

Figure 27. BAC modification steps to construct *Tg(akap12β:XFP)*.

(A-F) Schematic illustration of transgenesis. Preparation of HDR defective E.Coli containing Ch73-192G21 BAC vector (A). Insertion of HDR gene containing vector, pRedET, into E.Coli (B). Recombination of tol2 sequence into BAC (C). Recombination of XFP sequence into BAC (D). Preparation of modified BAC (E). Injection of modified BAC and transposase into 1-cell embryo (F)**.**

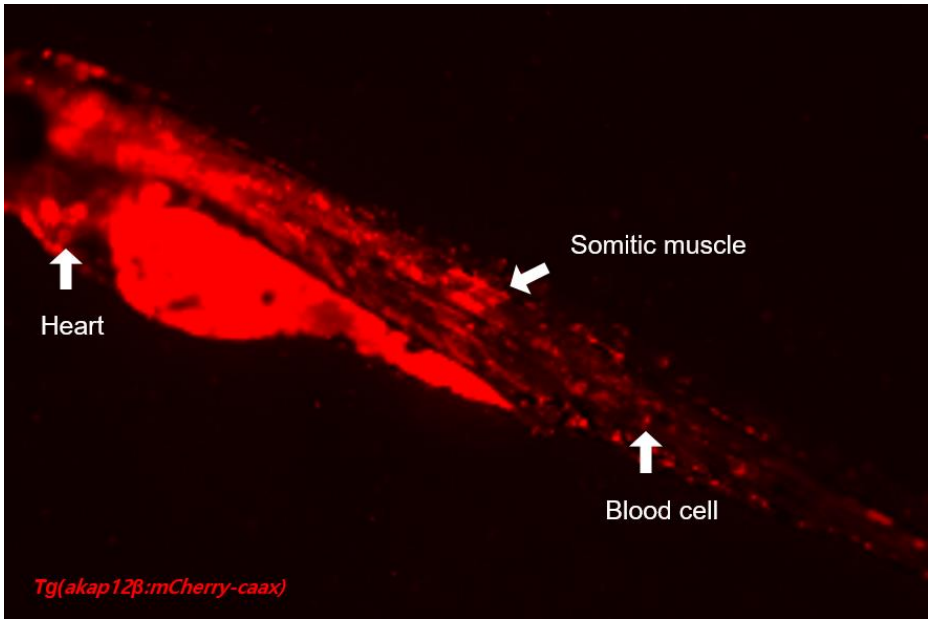

Figure 28. Establishment of *Tg(akap12β:mCherry-caax).*

Embryo injected with BAC(*akap12β:mCherry-caax)* was photographed at 30 hpf. Arrows indicate heart, blood cell and somatic muscle.

8. *cldn5a* is expressed in KV lineage cells.

The presence of Cldn5 at KV lumen was identified while investigating the role of *akap12* during KV development. To ascertain the serial expression of Cldn5 in KV development, the embryos were analyzed by immunofluorescence staining in *Tg(sox17:egfp*) embryos. Cldn5 expression was not significant in *sox17*-positive cells at 90% epiboly, when the DFCs migrate collectively (Fig. 29A). However, Cldn5 was stably expressed at the apical surface of the KV lumen from bud to 6 ss, while DFCs undergo apical clustering and lumen formation (Fig. 29B-29E). Since the two types of *cldn5*, *cldn5a* and *cldn5b,* were identified in zebrafish, the spatiotemporal expressions of them were examined by *in situ* hybridization and RT-PCR. *cldn5a* was highly expressed within the KV, marked by a red rectangle, and brain region, while *cldn5b* was highly expressed in the dorsal aorta and intersegmental vessels (Fig. 30). The results of the RT-PCR analysis indicated that *cldn5a* expression became detectable between 8 and 10 hpf, when the KV progenitor cells are detached from the enveloping layer and apically clustered (Fig. 31). In addition, the expression of Cldn5 in KV was efficiently suppressed by two types of *cldn5a* translation-blocking MO (Fig. 32). These data demonstrate that *cldn5a* is expressed at the apical surface of KV during KV lumen formation and expansion.

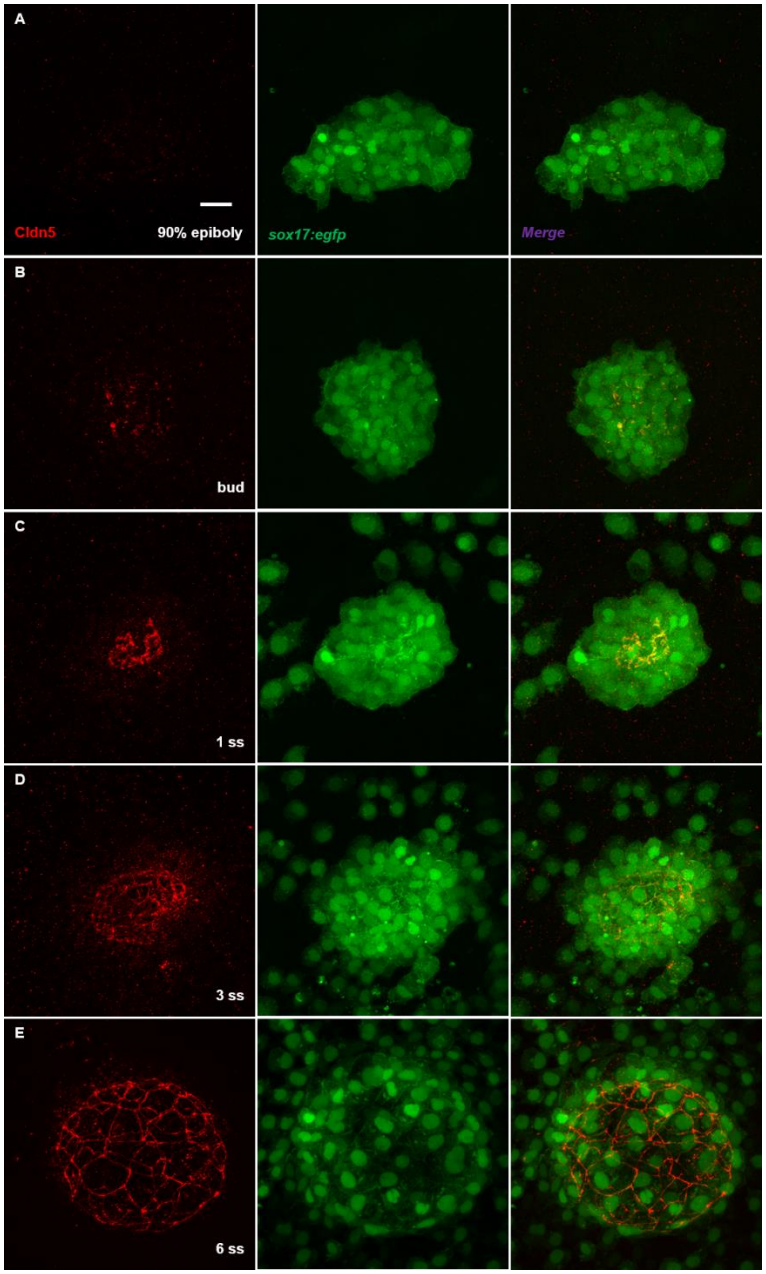

Figure 29. Expression patterns of Cldn5.

(A–E) Immunolabeling of Cldn5 in *sox17*-positive KV lineage cells from 90% epiboly to 6 ss. scale bar: 20μm

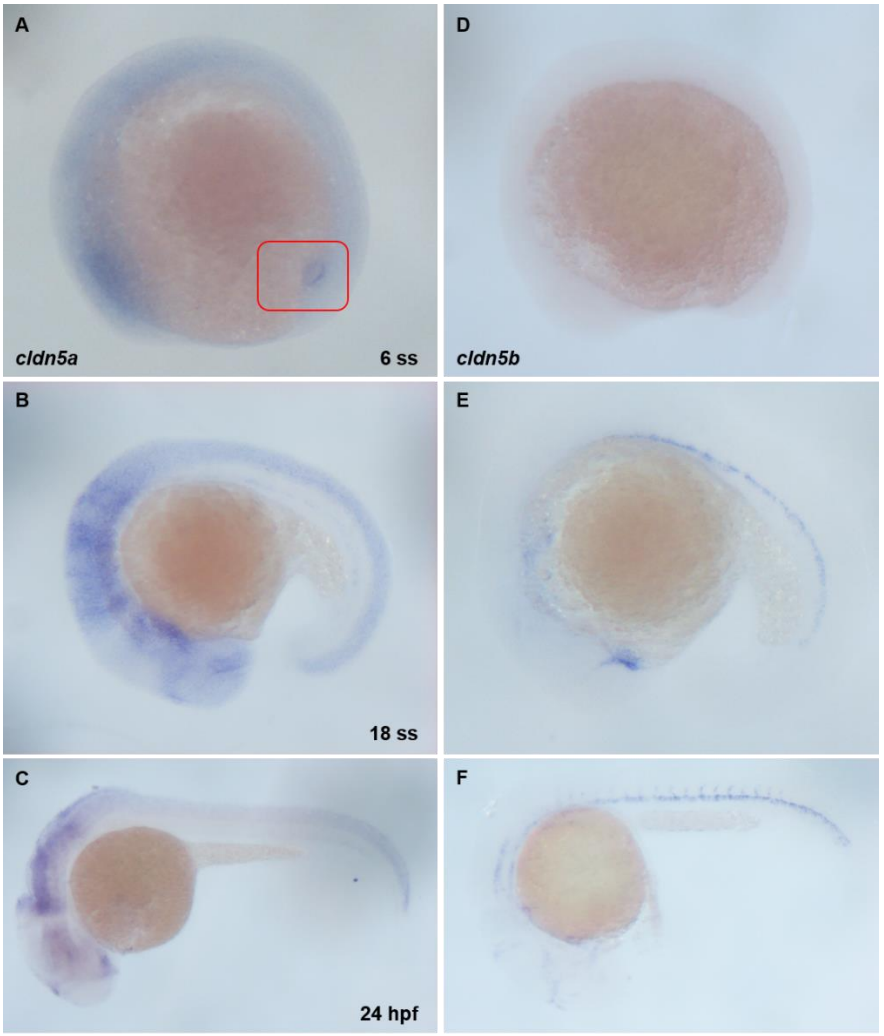

Figure 30. Expression patterns of *cldn5a* and *cldn5b*.

(A–C) *In situ* hybridization of *cldn5a.* Specific expression of *cldn5a* in Kupffer's vesicle at 6 ss, marked by a red rectangle (A). Expression of *cldn5a* in neuroepithelial cells at 18 ss and 24 hpf (B, C. respectively). **(D–F)** *In situ* hybridization of *cldn5b.* No obvious expression of *cldn5b* at 6 ss (D). Expression of *cldn5b* in dorsal aorta and intersegmental vessels at 18 ss and 24 hpf (E, F. respectively).

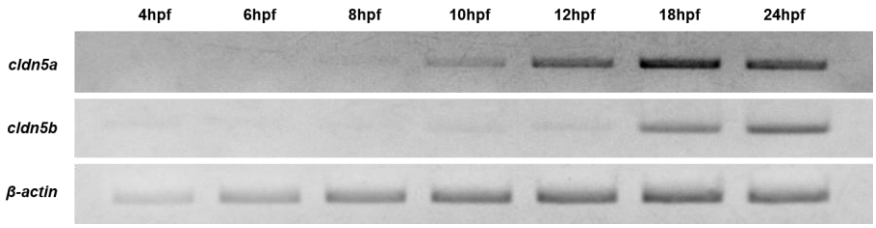

Figure 31. Serial expression of *cldn5a* and *cldn5b.*

Relative mRNA expression of *cldn5a, cldn5b,* and *β-actin* in sphere, shield, 75% epiboly, bud, 6 ss, 18 ss, and prim-5 staged embryos.

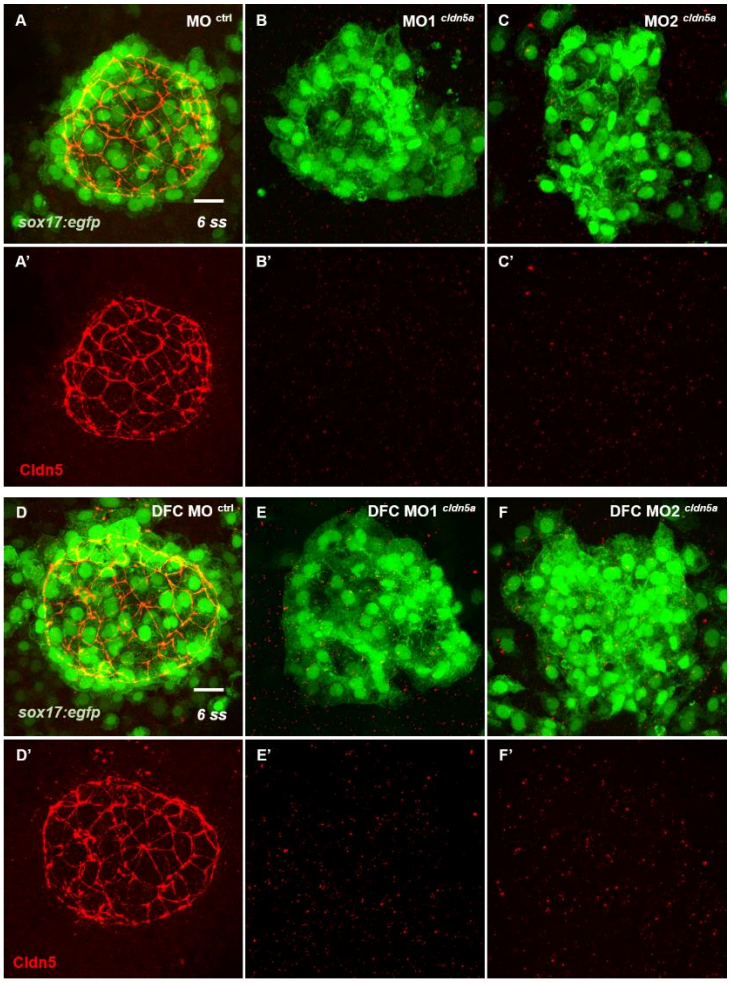

Figure 32. Expression of Cldn5 in KV was ablated by two types of *cldn5a* translation-blocking MO.

(A–F) Maximum intensity projection images of Cldn5 (red) and *sox17:egfp*-positive KV cells (green) in 6 ss embryos. Representative images of standard control MO injected embryo (A), *cldn5a* translation-blocking MO^1 injected embryo (B), *cldn5a* translation-blocking MO^2 injected embryo (C), DFC-specific control morphants (D), DFC-specific *cldn5a* MO^1 injected embryo (E), and DFC-specific *cldn5a* MO^2 injected embryo (F). Scale bar: 20 μm

9. Organ laterality was disrupted in *cldn5a* morphants.

Specific expression of *cldn5a* in KV lineage cells suggests that *cldn5a* might influence asymmetric organ development in zebrafish. Thus, the status of the heart, a representative asymmetric organ, was investigated by *in situ* hybridization of *cmlc1* in *cldn5a*-downregulated embryos. Two types of *cldn5a* MO efficiently blocked Cldn5 expression in KV (Fig. 32) and disrupted heart laterality (Fig. 33), without severe gross morphological defects (Fig. 34). Thus, I investigated the role of *cldn5a* using 5'-UTR-targeting MO[1], one of the two MO types. Compared with control morphants, *cldn5a* morphants exhibited significantly higher rates of the middle (42%) and reversed (18%) form of a heart (Fig. 35). To verify that the aberrant heart formation in *cldn5a* morphants was caused by *cldn5a* deficiency in KV lineage cells, I injected MO into the yolk at the 128 to 512-cell stage (DFC MO) for the exclusive reduction of *cldn5a* in DFCs and at the sphere to dome stage (Yolk MO) to confirm the effect of MO in the yolk and yolk syncytial layer. DFC *cldn5a* morphants showed a high rate of disrupted heart laterality (59%), whereas DFC-specific control, yolk-specific control, and yolk-specific *cldn5a* morphants showed a very low rate of heart laterality defects (Fig. 35). Finally, *mCherry* or *mCherry-cldn5a* mRNA with *cldn5a* MO was injected to rescue heart laterality defects in *cldn5a* morphants. In *cldn5a* morphants with *mCherry*, 31% of embryos showed a left-sided normal heart; however, 57% of *cldn5a* morphants with *mCherry-cldn5a* exhibited a normal heart status (Fig. 36). Thus, these data demonstrated that *cldn5a,* which is expressed in KV lineage cells, is functionally required for the left-right asymmetric development of the heart.

To validate how defective heart laterality in *cldn5a* morphants resulted from

the specific downregulation of *cldn5a* in KV lineage cells, I performed *in situ* hybridization of *spaw*, the *nodal*-related gene, which propagates through the left lateral plate mesoderm (LPM) from KV and determines the laterality of organs (Long et al., 2003; Wang and Yost, 2008). DFC *cldn5a* morphants showed bilateral (51%) and right-sided (7%) *spaw* expression, while only 2% of the DFC control morphants showed bilateral *spaw* expression (Fig. 37). Next, the expression of *dand5*, which is expressed around the KV and acts as a molecular barrier of *spaw,* was investigated (Hashimoto et al., 2004; Lopes et al., 2010). *dand5* is expressed bilaterally around KV at 6 ss and is subsequently predominant on the right. Expression patterns of *dand5* at 6 ss in DFC control morphants were mostly normal with a horseshoe shape; however, most DFC *cldn5a* morphants showed abnormal (89%) *dand5* expression (Fig. 38). In addition, *dand5* expression was not predominant on the right side of KV in most of DFC *cldn5a* morphants (Fig. 38). Furthermore, quantitative analysis of *dand5* revealed the significant reduction in DFC *cldn5a* morphants (0.313 ± 0.018). Thus, these data showed that the disrupted heart laterality is correlated with aberrant expression of asymmetric signals

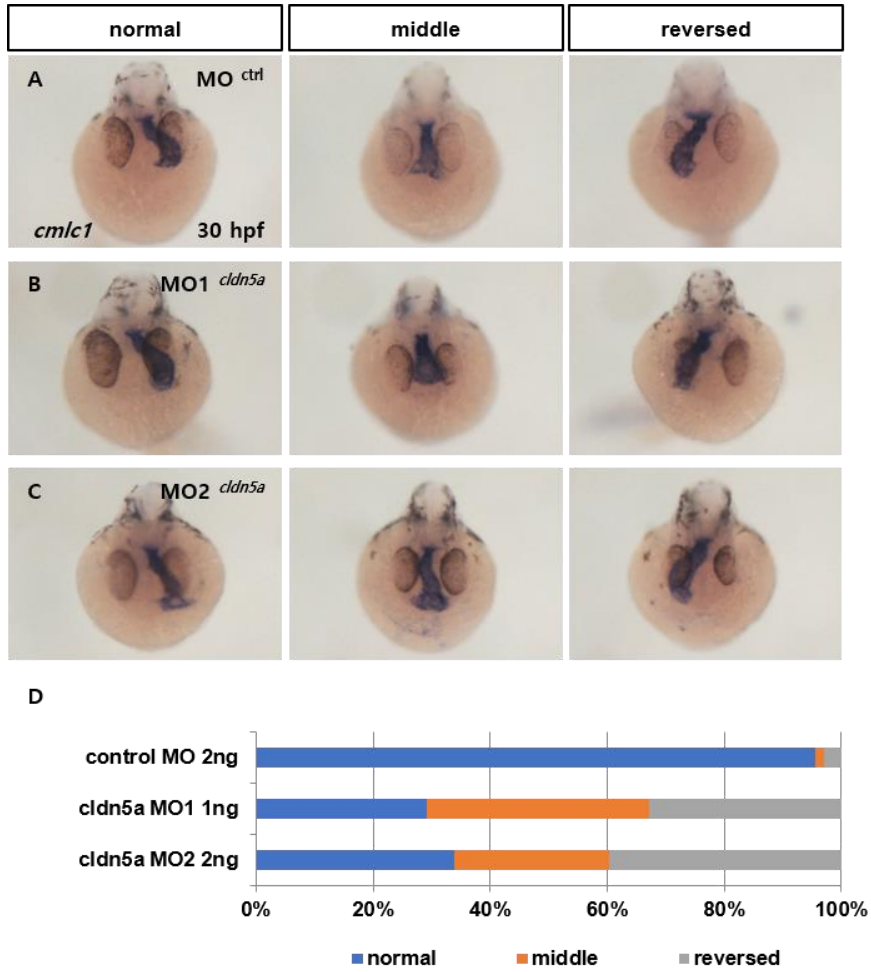

Figure 33. Heart laterality defects of *cldn5a* MO[1] and MO[2] injected embryos.

(A–C) Visualization of heart by *in situ* hybridization of *cmlc1* in 30 hpf embryos. Representative images of control morphants (A), *cldn5a* MO[1] injected embryo (B), and *cldn5a* MO[2] injected embryo (C). **(D)** Statistical stacked bar graph (blue; normal, orange; middle, grey; reversed, control morphants; n = 68, *cldn5a* MO[1] injected embryos; n = 55, and *cldn5a* MO[2] injected embryos; n = 53).

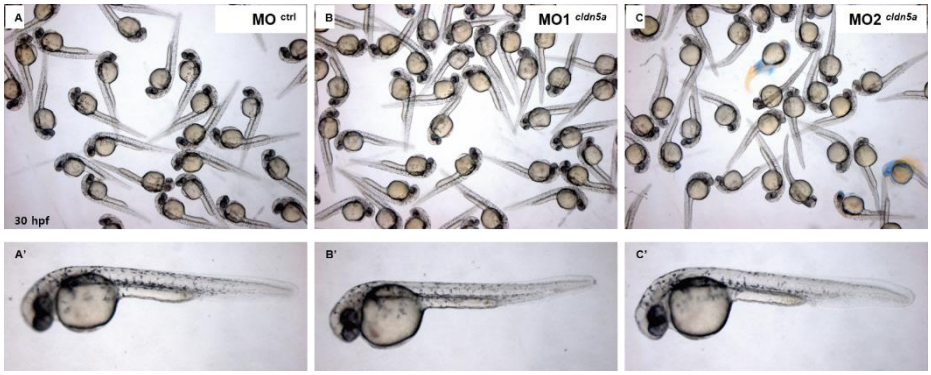

Figure 34. Gross morphology of *cldn5a* MO[1] and MO[2] injected embryos.

(A–C) Gross morphology of control morphants (A), *cldn5a* MO[1] injected embryo (B), and *cldn5a* MO[2] injected embryo (C).

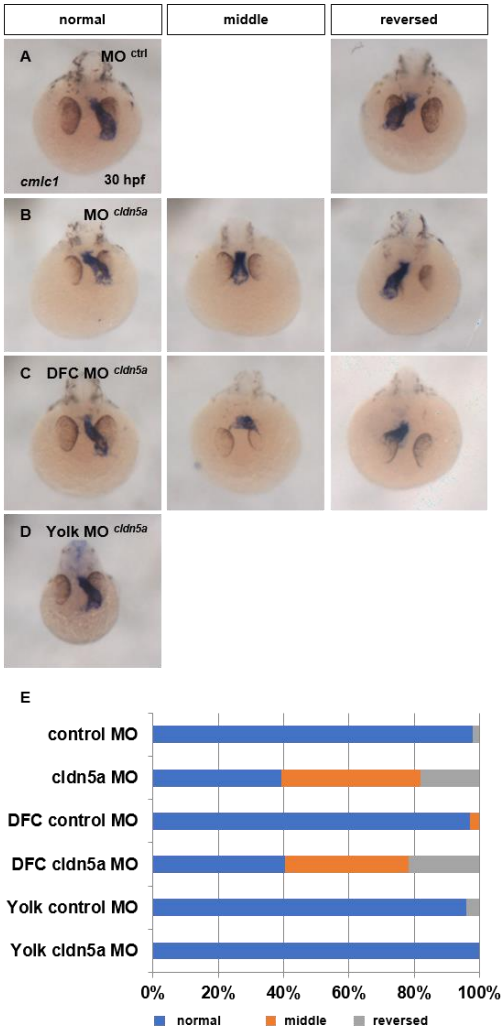

Figure 35. Laterality of heart was disrupted in *cldn5a* morphants.

(A–C) Visualization of heart by i*n situ* hybridization of *cmlc1* in 30 hpf embryos. Representative images of control morphants (A), *cldn5a* morphants (B), and DFC *cldn5a* morphants (C). **(D)** Statistical stacked bar graph (dark grey; normal, grey; middle, white; reversed, control morphants; n = 45, *cldn5a* morphants; n = 33, DFC control morphants; n = 71, DFC *cldn5a* morphants; n = 37).

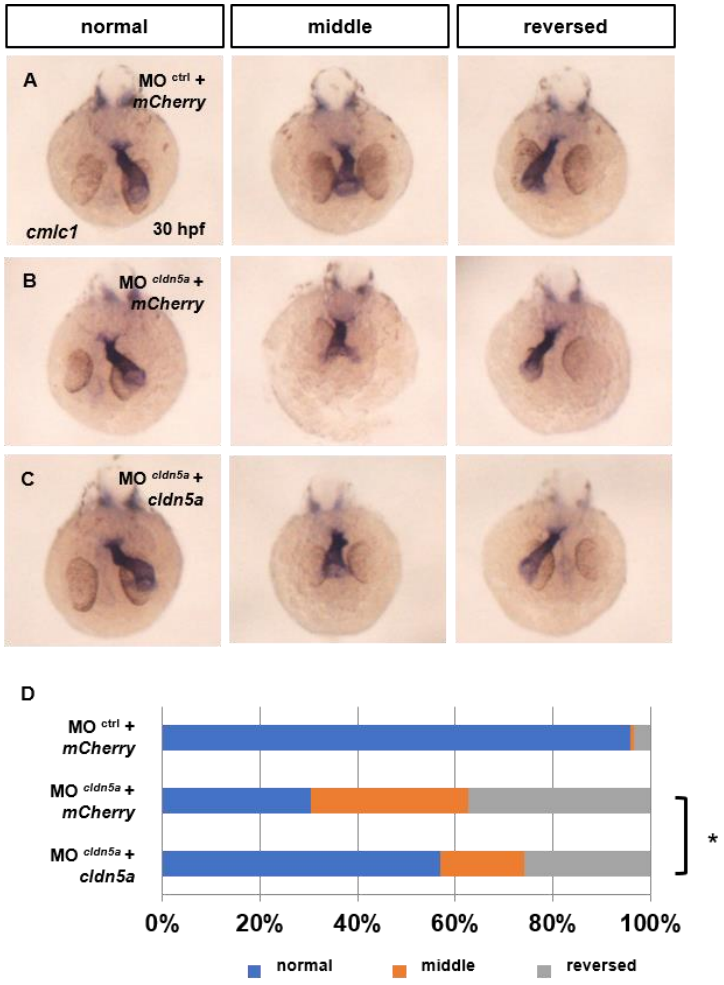

Figure 36. Disrupted heart laterality was rescued by exogenous *cldn5a* mRNA in *cldn5a* morphants.

(A–C) Visualization of a heart by *in situ* hybridization of *cmlc1* in 30 hpf embryos. Representative images of control morphants with *mCherry* (A), *cldn5a* morphants with *mCherry* (B), *cldn5a* morphants with *mCherry-cldn5a* (C). **(D)** Stacked bar graph (blue; normal, orange; middle, grey; reversed, control morphants with *mCherry*; n = 132, *cldn5a* morphants with *mCherry*; n = 111, *cldn5a* morphants with *mCherry-cldn5a*; n = 115). * depicts $p < 0.05$.

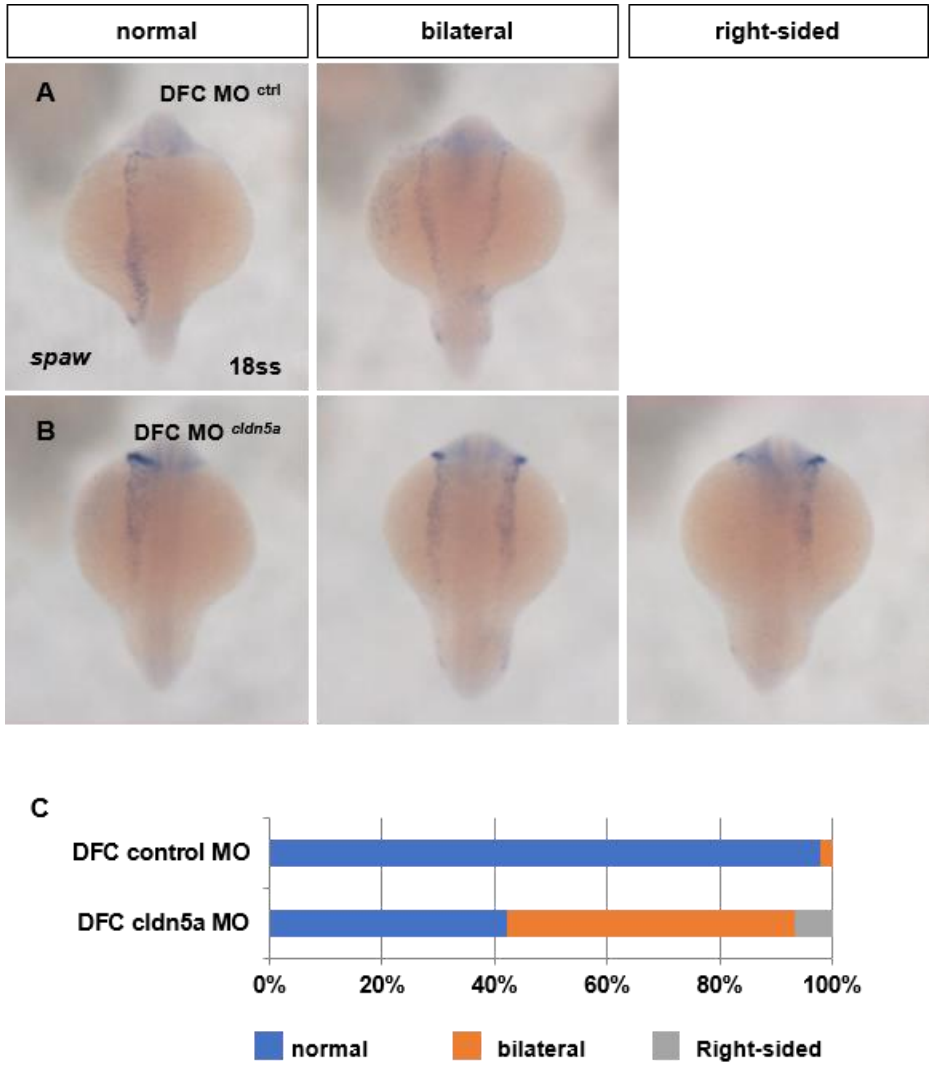

Figure 37. Expression of *spaw* was disrupted in DFC *cldn5a* morphants.

(A, B) Visualization of *spaw* by *in situ* hybridization in 18 ss embryos. Representative images of DFC control morphants (A) and DFC *cldn5a* morphants (B). **(C)** Statistical stacked bar graph (dark grey; normal, grey; bilateral, white; right-sided, DFC control morphants; n = 48, DFC *cldn5a* morphants; n = 45).

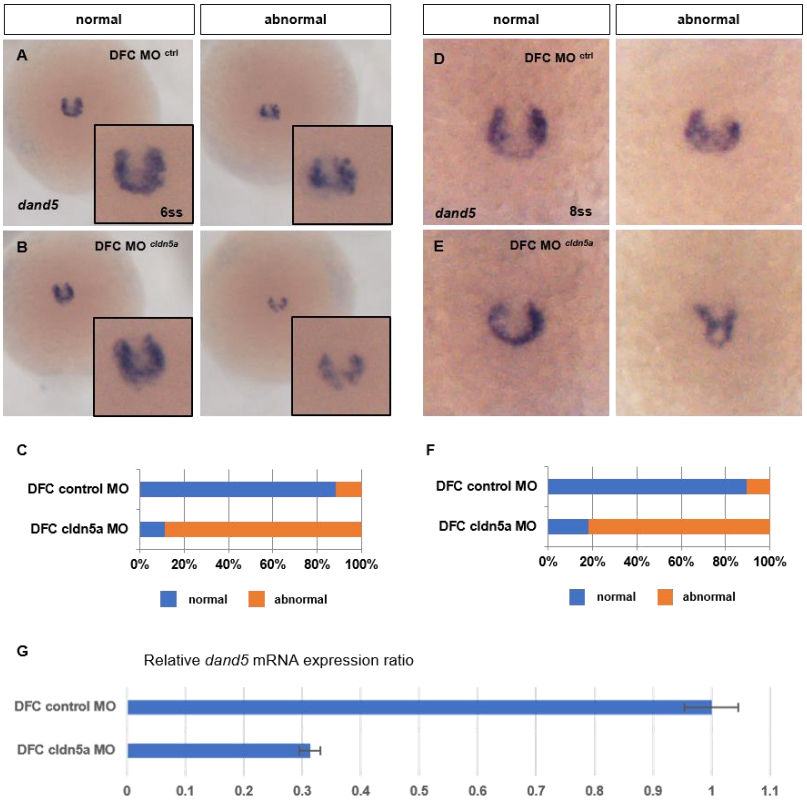

Figure 38. Expression of *dand5* was disrupted in DFC *cldn5a* morphants. **(A–B)** Visualization of *dand5* by *in situ* hybridization in 6 ss embryos. Representative images of DFC control morphants (A) and DFC *cldn5a* morphants (B). **(C)** Stacked bar graph (blue; normal, orange; abnormal, DFC control morphants; n = 26, DFC *cldn5a* morphants; n = 36). **(D–E)** Visualization of *dand5* by *in situ* hybridization in 8 ss embryos. Representative images of DFC control morphants (D) and DFC *cldn5a* morphants (E). **(F)** Stacked bar graph (blue; normal, orange; abnormal, DFC control morphants; n = 76, DFC *cldn5a* morphants; n = 82). **(G)** Relative *dand5* mRNA expression in DFC *cldn5a* morphants versus DFC control morphants at 8 ss. Error bars indicate s.e.m.

10. *cldn5a* is required for proper inflation of KV lumen.

Ciliogenesis is an important event in asymmetric signal transmission. Motile cilia generate unidirectional fluid flow, and the leftward signal is activated by intracellular Ca^{2+} release (Bisgrove et al., 2005; Francescatto et al., 2010; Jurynec et al., 2008; Schottenfeld et al., 2007). In addition, it was reported that cilia-driven fluid flow is important for *dand5* expression (Lopes et al., 2010; Sampaio et al., 2014). Thus, I investigated the status of cilia in DFC *cldn5a* morphants by immunostaining of acetylated tubulin. The numbers of cilia were 62.12 ± 3.18 and 31.57 ± 3.62 per embryo in DFC control and *cldn5a* morphants, respectively (Fig. 39). Although the number of cilia decreased in DFC *cldn5a* morphants, the average length of cilia in DFC *cldn5a* morphants (4.30 ± 0.050 μm) was comparable to that of the DFC control morphants (4.24 ± 0.075 μm) (Fig. 39). Since a common feature of the downregulation of ciliogenesis factors in the KV was a shortened cilia length as well as a decreased cilia number (Bisgrove et al., 2012; Krock and Perkins, 2014; Liu et al., 2011; Oishi et al., 2006; Zhang et al., 2012), it is suspected that *cldn5a* might not be directly involved in ciliogenesis. In this regard, I further identified the reduction of *sox17:egfp*-positive KV lineage cells in DFC *cldn5a* morphants from the bud to 10 ss (Fig. 40). The number of *sox17:egfp*-positive cells in DFC *cldn5a* morphants at the bud stage was comparable to that of DFC control morphants. In addition, though the difference of the number of *sox17:egfp*-positive KV cells between the DFC control and *cldn5a* morphants started to increase at 3 ss, it did not exceed 25% until 10 ss. This was still less than the reduced rate of cilia in DFC *cldn5a* morphants (49%) (Fig. 39). Instead, single plain images showed that some *sox17:egfp*-positive cells did not participate in KV lumen

formation and that the cilia were only localized near the small KV lumen in DFC *cldn5a* morphants (Fig. 39). Thus, these data suggest that the decreased number of cilia within smaller KV lumen might influence the expression and asymmetry of *dand5*.

I observed that the KV lumen was small in DFC *cldn5a* morphants; accordingly, I investigated the role of *cldn5a* in KV lumen formation and expansion. First, *sox17* (a marker for DFC specification) promoter-induced EGFP was stained at the 75% epiboly stage, when the DFCs collectively migrate towards the vegetal pole. In both DFC control and DFC *cldn5a* morphants, each DFC cluster was normally maintained without fragmentation (Fig. 41), indicating that DFC specification was not affected by *cldn5a*. Next, I measured the KV lumen area over time. Fortunately, the localization of ZO-1 at the luminal surface of the KV lumen was not affected by the loss of *cldn5a* (Fig. 42). Thus, I measured the area enclosed by ZO-1 in Z-stack images by maximum intensity projection. However, since the morphology of the ZO-1-positive KV lumen in DFC *cldn5a* morphants was a distorted circle, I used the Closed Beizer tool in ZEN software which automatically calculates the enclosed area, rather than obtaining KV ^{max}, which multiplies the length of the longest radius. The KV lumen areas of DFC *cldn5a* morphants and DFC control morphants were 2599 ± 207.3 μm^2 and 5798 ± 315.1 μm^2 at 6 ss, 3286 ± 159.4 μm^2 and 7157 ± 281.0 μm^2 at 8 ss, and 3526 ± 348.9 μm^2 and 7515 ± 446.0 μm^2 at 10 ss, respectively (Fig. 43). Considering the KV lumen area and the number of cells in the KV together (Fig. 40), these data suggest that the KV lumen was not fully inflated in DFC *cldn5a* morphants. In addition, I injected *mCherry* or *mCherry-cldn5a* mRNA with *cldn5a* morpholino to rescue the KV lumen area

in *cldn5a* morphants. Compared with *cldn5a* morphants with *mCherry* (lumen area: 2183 ± 176.3 μm^2), *cldn5a* morphants with *mCherry-cldn5a* exhibited recovery of the KV lumen area (4216 ± 274.2 μm^2) (Fig. 44).

Claudins are major constituents of tight junction strands and previous papers have reported the size-selective loosening of blood-brain barrier in *cldn5* knockout mice and an under-inflated ventricular lumen in *cldn5a* morphant zebrafish (Nitta et al., 2003; Zhang et al., 2010). Thus, I assumed that paracellular permeability was increased and fluid influx probably leaked through the intercellular space between the KV epithelial cells. Thus, recovery of the malformed KV lumen size in DFC *cldn5a* morphants by increasing the fluid influx was verified. From 90% epiboly to 6 ss, zebrafish embryos were treated with a mixture of 10 μM forskolin and 40 μM IBMX which increases fluid secretion through Cftr by elevating the intracellular levels of cAMP by activating adenylyl cyclase and inhibiting phosphodiesterase activity, respectively (Compagnon et al., 2014; Navis et al., 2013; Roxo-Rosa et al., 2015). Combined treatment with forskolin and IBMX successfully increased the KV lumen area in DFC control morphants (7020 ± 423.0 versus 5410 ± 307.9 μm^2, Fig. 45). However, the combined treatment failed to increase the KV lumen area in DFC *cldn5a* morphants (2117 ± 275.0 versus 2266 ± 347.3 μm^2), indicating that the reinforced fluid influx leaked through the intercellular space between weakly-adhered KV epithelial cells in the absence of *cldn5a*. Thus, I suggest that *cldn5a* is required for KV lumen inflation by supporting paracellular junctions within KV epithelial cells.

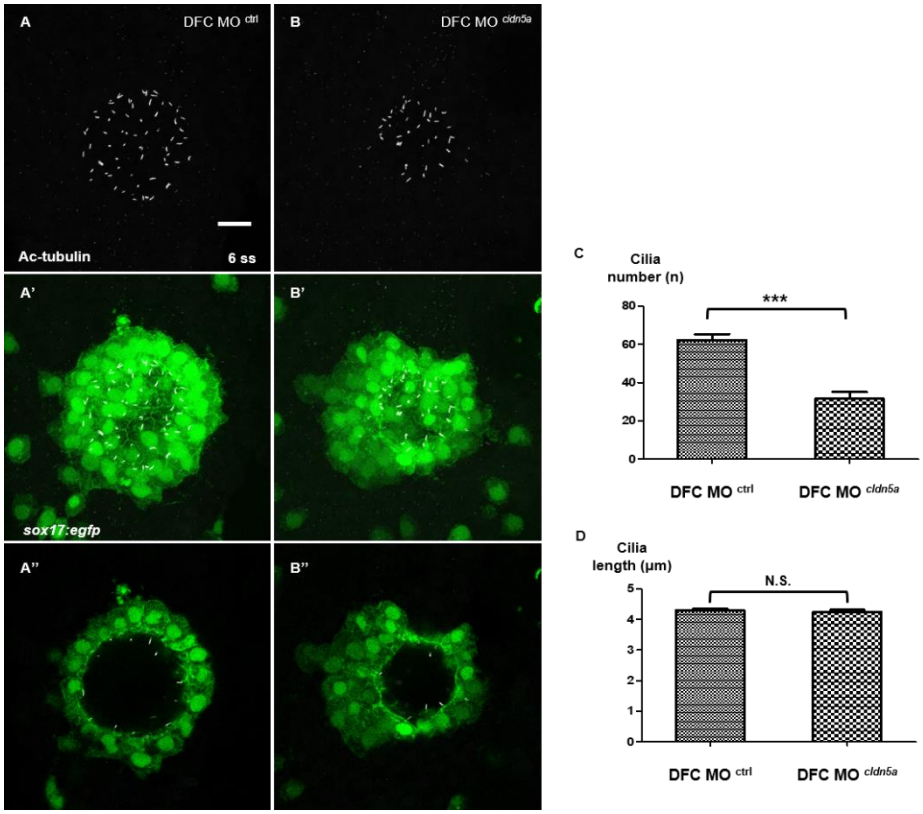

Figure 39. Decreased number of cilia in partially formed KV lumen.

(A–A', B–B') Maximum intensity projection images of acetylated tubulin (grey) and *sox17:egfp*-positive KV cells (green) in 6 ss embryos. Representative images of DFC control morphants (A), and DFC *cldn5a* morphants (B). **(A", B")** Single plane images of acetylated tubulin (grey) and *sox17:egfp*-positive KV cells (green) in 6 ss embryos. **(C)** Statistical column bar graph of cilia number (DFC control morphants; n = 25, DFC *cldn5a* morphants; n = 30) **(D)** Statistical column bar graph of cilia length (DFC control morphants; n = 314, DFC *cldn5a* morphants; n = 128). *** depicts $p < 0.001$, N.S. (not significant) depicts $p > 0.05$. Error bars indicate s.e.m. Scale bar: 20 µm

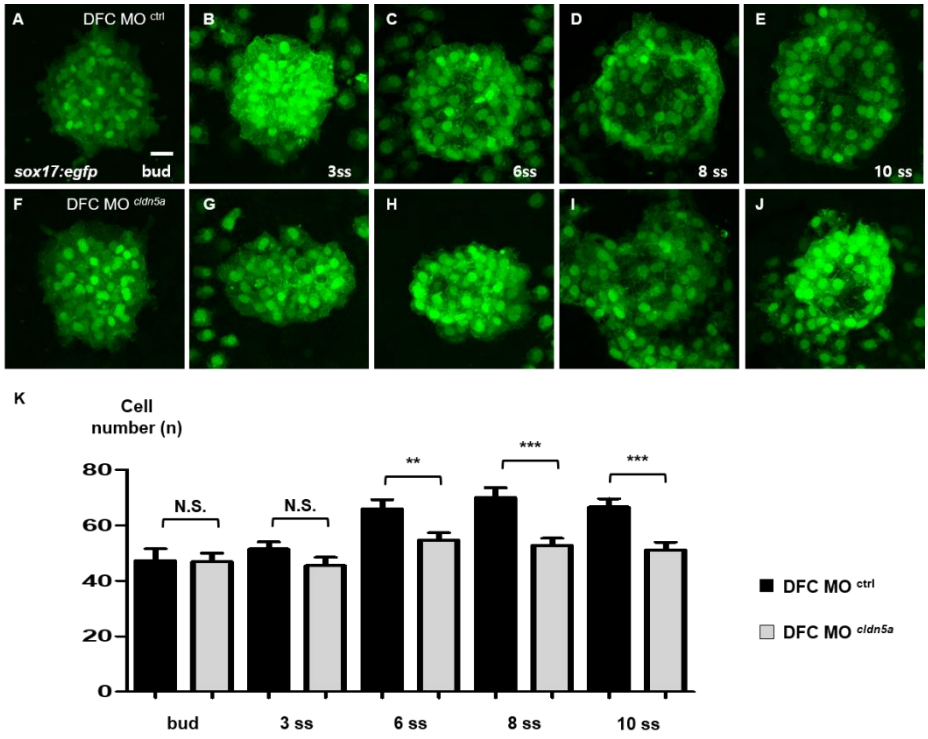

Figure 40. Status of DFC cluster and KV consisting cell number in DFC *cldn5a* morphants.

(A–J) Maximum intensity projection images of *sox17:egfp*-positive KV lineage cells in DFC control and *cldn5a* morphants from bud to 10 ss. (A–E) Representative images of the DFC control morphants. (F–J) Representative images of the DFC *cldn5a* morphants. **(K)** Statistical column bar graph (DFC control morphants at bud; n = 18, 3 ss; n = 25, 6 ss; n = 23, 8 ss; n = 19, 10 ss; n = 16, DFC *cldn5a* morphants at bud; n = 18, 3 ss; n = 30, 6 ss; n = 31, 8 ss; n = 20, 10 ss; n = 19). *** depicts $p < 0.001$, ** depicts $p < 0.01$, N.S. depicts $p > 0.05$. Error bars indicate s.e.m. Scale bar: 20 μm

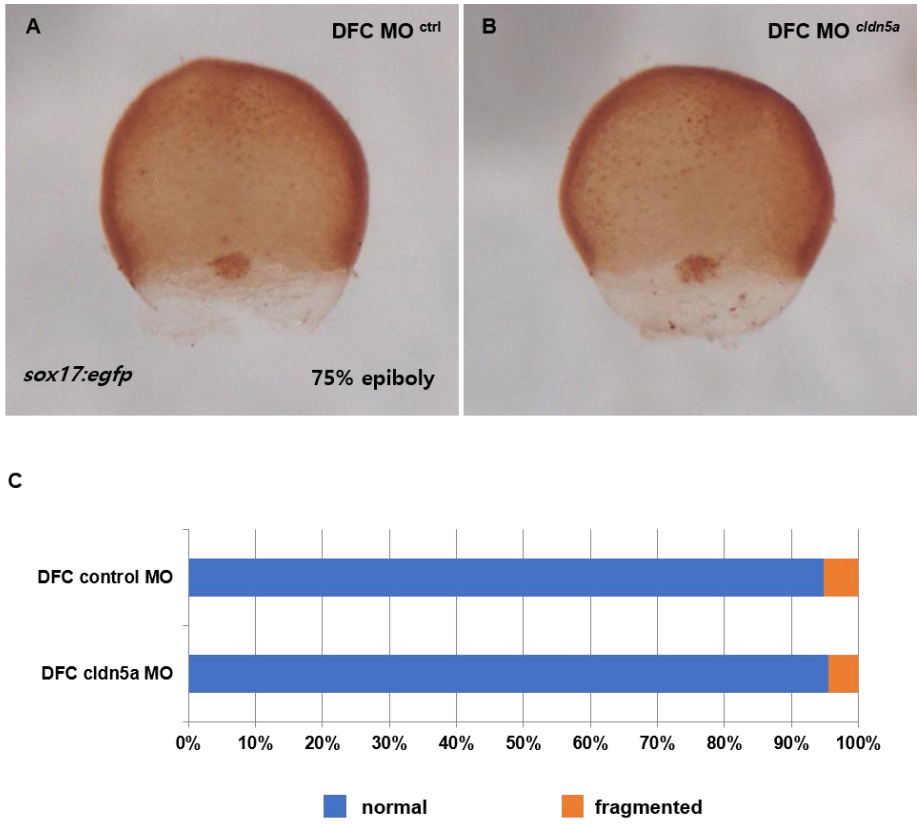

Figure 41. Cluster of DFCs was not fragmented in DFC *cldn5a* morphants. **(A, B)** Visualization of DFCs by immunostaining of *sox17*-promoter induced EGFP in 75% epiboly embryos. Representative images of DFC control morphants (A) and DFC *cldn5a* morphants (B). **(C)** Statistical stacked bar graph (dark grey; normal, grey; fragmented, DFC control morphants; n = 22, DFC *cldn5a* morphants; n = 38).

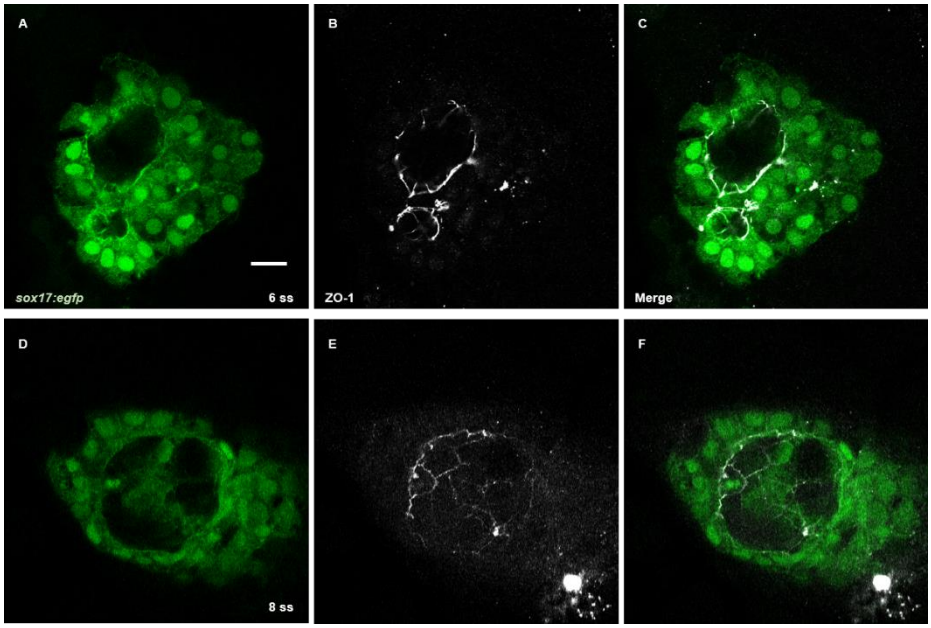

Figure 42. Localization of ZO-1 was not altered in DFC *cldn5a* morphants. **(A–F)** Single plane images of ZO-1 (grey) and *sox17:egfp*-positive KV cells (green) in 6 ss and 8 ss embryos. Representative images of DFC *cldn5a* morphants at 6 ss (A–C) and 8 ss (D–F). Scale bar: 20 μm

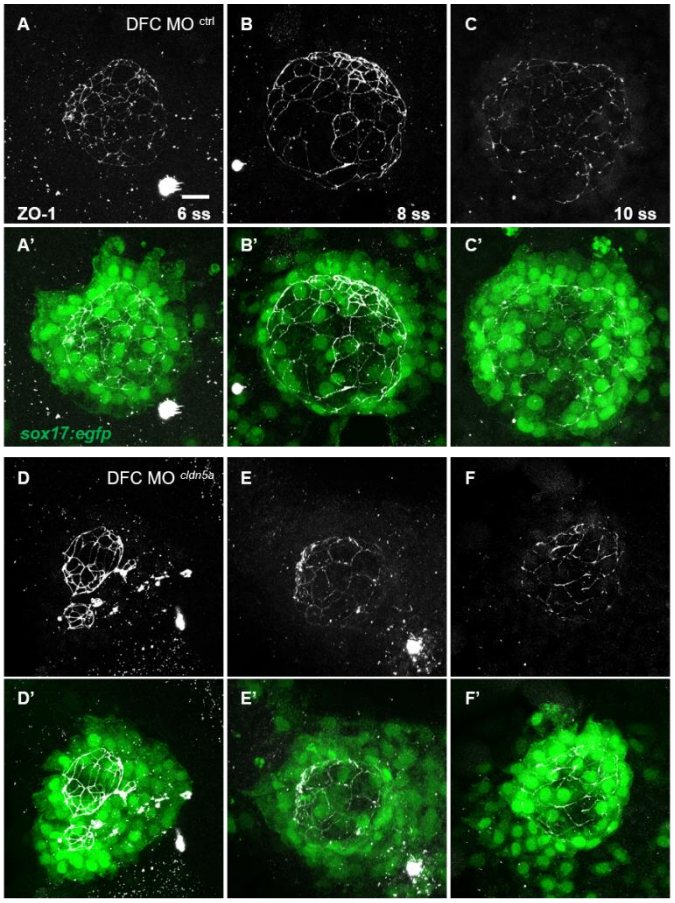
A
DFC MO ctrl
B
C
ZO-1
6 ss
8 ss
10 ss
A'
B'
C'
sox17:egfp
D
DFC MO cldn5a
E
F
D'
E'
F'

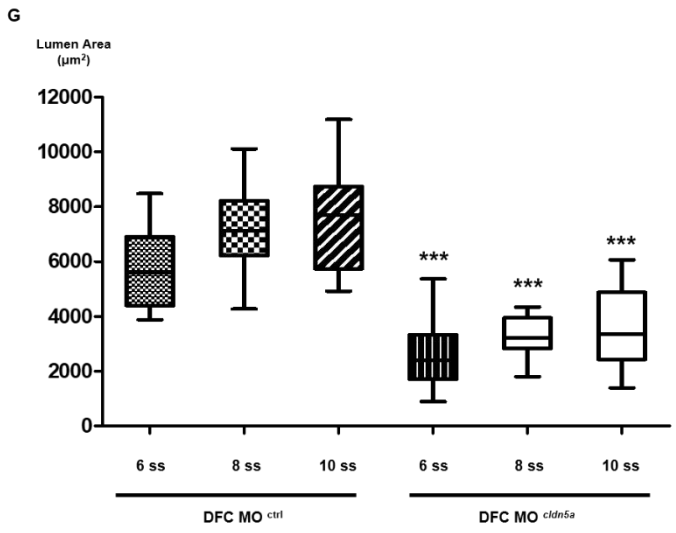
G
Lumen Area
(μm²)
12000
10000
8000
6000
4000
2000
0
***
***
***
6 ss
8 ss
10 ss
6 ss
8 ss
10 ss
DFC MO ctrl
DFC MO cldn5a

Figure 43. Downregulation of *cldn5a* resulted in defective KV lumen in zebrafish.

(A–F) Maximum intensity projection images of ZO-1 (grey) and *sox17:egfp*-positive KV cells (green) in 6 ss, 8 ss and 10 ss embryos. Representative images of the DFC control morphants (A–C) and DFC *cldn5a* morphants (D–F). **(G)** Statistical box and whisker graph (DFC control morphants at 6 ss; n = 20, DFC control morphants at 8 ss; n = 31, DFC control morphants at 10 ss; n = 15, DFC *cldn5a* morphants at 6 ss; n = 28, DFC *cldn5a* morphants at 8 ss; n = 21, DFC *cldn5a* morphants at 10 ss; n = 18). Scale bar: 20 μm

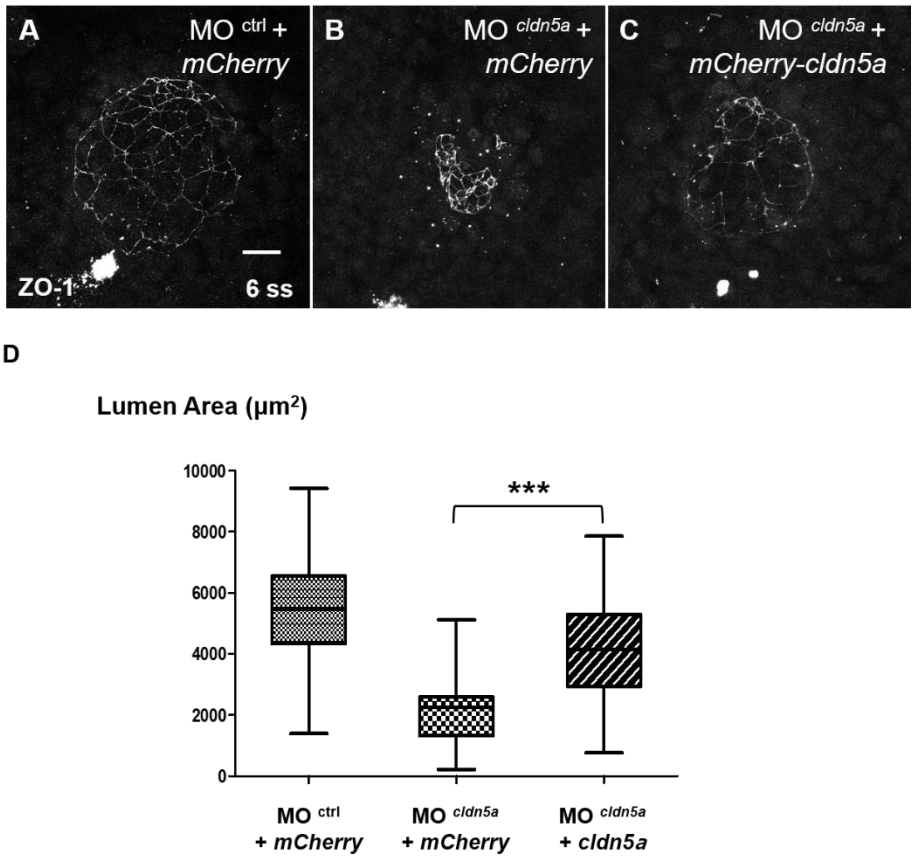

Figure 44. KV lumen area of *cldn5a* morphants was restored by exogenous *cldn5a* mRNA.

(A–C) Maximum intensity projection images of ZO-1 in 6 ss embryos. Representative images of control morphants with *mCherry* (A), *cldn5a* morphants with *mCherry* (B), and *cldn5a* morphants with *mCherry-cldn5a* (C). **(D)** Statistical box and whisker graph (control morphants with *mCherry*; n = 25, *cldn5a* morphants with *mCherry*; n = 39, *cldn5a* morphants with *mCherry-cldn5a*; n = 43) *** depicts $p < 0.001$. Error bars indicates s.e.m. Scale bar: 20 µm

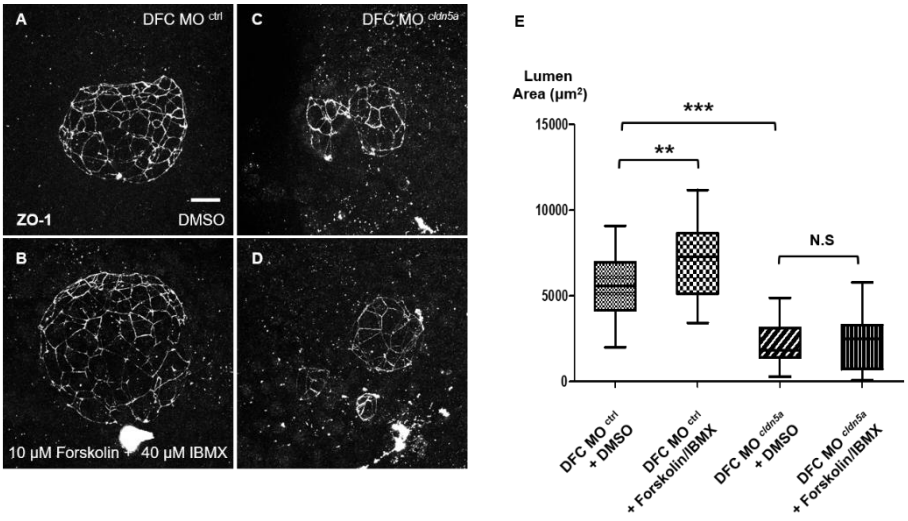

Figure 45. Treatment of forskolin and IBMX failed to recover the KV lumen size in DFC *cldn5a* morphants.

(A–D) Maximum intensity projection images of ZO-1 in 6 ss embryos. Representative images of DFC control morphants treated with DMSO (A) or forskolin/IBMX (B). Representative images of DFC *cldn5a* morphants treated with DMSO (C) or forskolin/IBMX (D). **(E)** Statistical column bar graph (DFC control morphants with DMSO; n = 30, DFC control morphants with forskolin/IBMX; n = 28, DFC *cldn5a* morphants with DMSO; n = 19, DFC *cldn5a* morphants with forskolin/IBMX; n = 22). *** depicts $p < 0.001$, ** depicts $p < 0.01$, N.S. depicts $p > 0.05$. Error bars indicate s.e.m. Scale bar: 20 μm

11. Establishment of *cldn5a* crispant.

In the present study, I performed morpholino-based approach to reveal the role of *cldn5a* in zebrafish. Two types of *cldn5a* morphants showed similar phenotypes of disrupted heart laterality and exogenous RNA rescued the *cldn5a* morpholino-induced phenotypes. Several recent papers reported that genome-engineered mutants failed to recapitulate the morpholino-induced phenotypes (Kok et al., 2015; Novodvorsky et al., 2015; Place and Smith, 2017). Although genetic compensation might be induced in mutant embryos (Rossi et al., 2015), morpholino-based studies should be carefully considered whether their phenotypes are driven by off-target effects. In this regard, I conducted CRISPR/Cas9-mediated *cldn5a* mutation and analyzed whether heart laterality might be affected in *cldn5a* crispants (Jao et al., 2013).

First, I constructed two types of *cldn5a*-targeting guide RNA (gRNA) chimera which directs Cas9 to forward and reverse strands of the genomic *cldn5a*, respectively (Fig. 46). Then, 40 pg of each gRNA and 80 pg of *cas9* mRNA were injected into 1-cell staged embryos. Although the *cldn5a* morphants did not show the severe defects in gross development, *cldn5a* gRNA1 injected crispants exhibited morphogenetic problem (Fig. 47). Then, the heart status was examined in 30 hpf embryos (Fig. 48). 61% of gRNA2 and *cas9* mRNA injected embryos showed the disrupted heart laterality, however, only 18% of gRNA1 and *cas9* mRNA injected embryos showed the laterality defects of heart. Then, I selected 10 embryos of each group and carried out T7 endonuclease I assay of *cldn5a* genomic DNA amplicon (Fig. 49). Interestingly, only gRNA2 and *cas9* mRNA injected group of embryos showed the *cldn5a* mutation, indicating that the morphological problem in gRNA1 and *cas9*

mRNA injected embryos might be arose from off-target mutation. Then, I cloned the *cldn5a* genomic DNA of gRNA2 and *cas9* mRNA injected embryos to identify whether *cldn5a* was genuinely mutated. 4 out of 7 of them had deletion mutations near the gRNA2 targeting sequence. Thus, these data strengthen the *cldn5a* morpholino-based studies that *cldn5a* regulates organ laterality by modulating KV lumen formation.

A

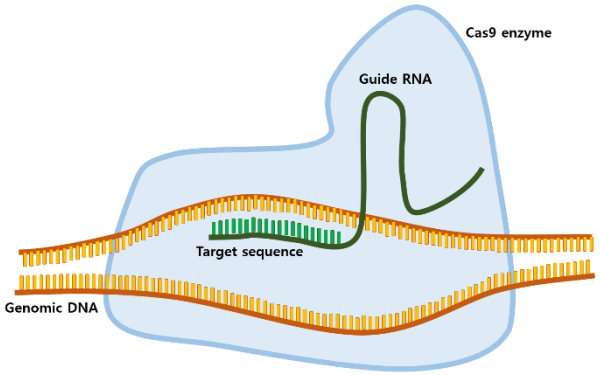

B

[1]ATGGCCTCCGCGGCTTTGGAGCTCCTGGGTCTGATCCTGTGCGTCTGCGGGACGCTTTTGGAGATGGT
GGCCTGCGGGCTGCCCACCTGGAAGGTCACCGCCTTCATCGAGGCCAACATCGTGGTCGCGCAGACCA
TCTGGGACGGCCTG[150]

cldn5a gRNA1 sequence : GGTCTGATCCTGTGCGTCTG

cldn5a gRNA2 sequence : GGTCTGCGCGACCACGATGT

Figure 46. CRISPR/Cas9-mediated *cldn5a* targeting gRNA sequences.

(A) Illustration of site-directed mutagenesis by CRISPR/Cas9 method **(B)** Partial nucleotide sequences of *cldn5a* coding sequence (1-150 among 648) and two types of *cldn5a* targeting gRNA sequences.

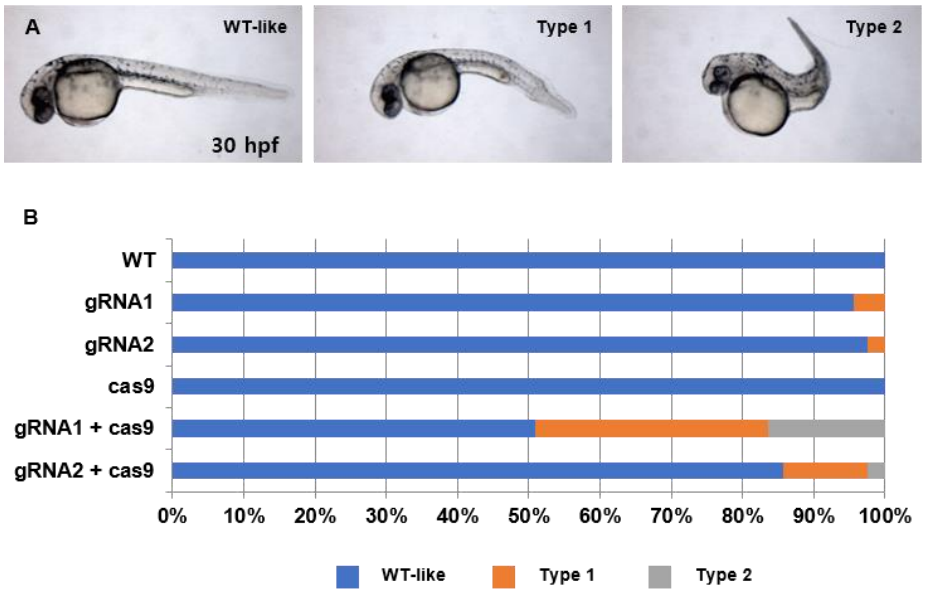

Figure 47. Gross morphology of *cldn5a* crispants.

(A) Representative images of WT-like, type1 and type2 embryos at 30 hpf. **(B)** Stacked bar graph (blue; WT-like, orange; type1, grey; type2, WT; n = 24, 40 pg of gRNA1 injected embryos; n = 45, 40 pg of gRNA2 injected embryos; n = 41, 80 pg of *cas9* mRNA injected embryos; n = 52, 40 pg of gRNA1 and 80 pg of *cas9* mRNA injected embryos; n = 55, 40 pg of gRNA2 and 80 pg of *cas9* mRNA injected embryos; n = 42).

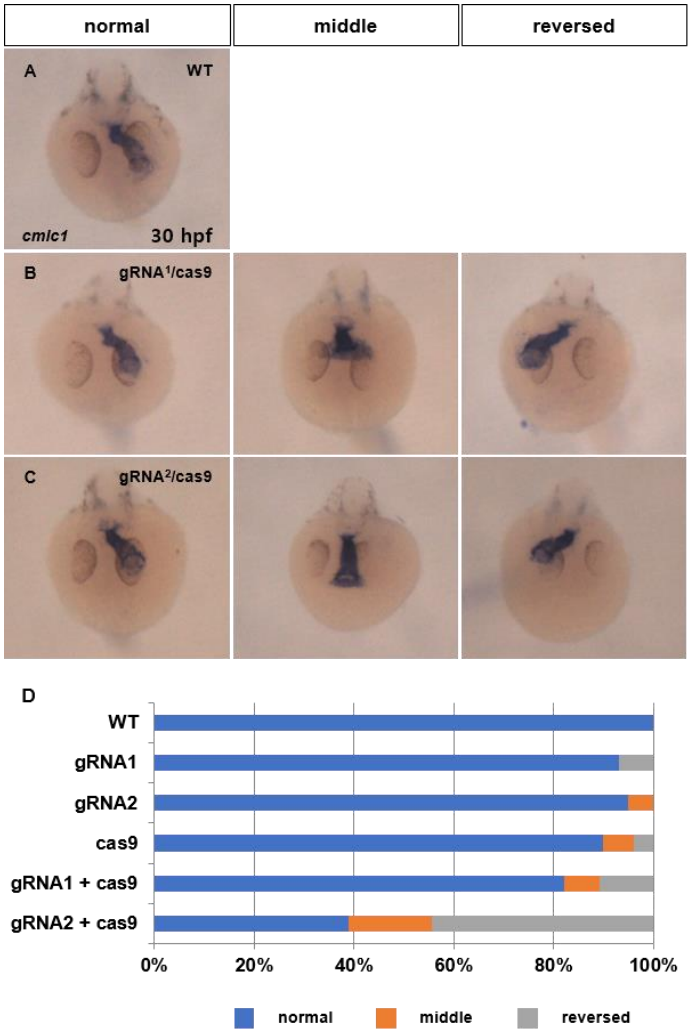

Figure 48. Laterality of heart was disrupted in *cldn5a* crispants.

(A–C) Visualization of a heart by *in situ* hybridization of *cmlc1* in 30 hpf embryos. Representative images of WT (A), gRNA1 crispants (B), and gRNA2 crispants (C). **(D)** Stacked bar graph (blue; normal, orange; middle, grey; reversed, WT; n = 24, only gRNA1 injected embryos; n = 43, only gRNA2 injected embryos; n = 40, only *cas9* mRNA injected embryos; n = 52, gRNA1 crispants; n = 28, gRNA2 crispants; n = 36).

Figure 49. Mutation of *cldn5a* gene in *cldn5a* crispants.

(A) T7E1 analysis of *cldn5a* crispants. **(B)** Representative mutations of *cldn5a* gene in gRNA2 crispants.

DISCUSSION

In the present study, I identified that *akap12* was expressed in cluster of DFCs. However, *akap12β* expression in DFCs was not confirmed by ISH with specific probe. In general, specific riboprobe for ISH should be 250~1500 bases for its effective experimental outcome. Unfortunately, specific nucleotide sequences of *akap12β* mRNA except the common region with *akap12α* mRNA is only 32 bases. Thus, I injected the specific MOs for *akap12α* or *akap12β,* and measure the relative amount of *akap12*. Interstingly, the mRNA expression level of *akap12* in *akap12β* morphants was significantly reduced but, that in *akap12α* morphants was almost unchanged at 75% epiboly, when the DFCs collectively migrate toward vegetal pole (Fig. 7). For this reason, I speculated that *akap12β* might be the major isofoms of *akap12* during collective migation of DFCs.

In DFC *akap12β* morphants, organ laterality was disrupted and KV was malformed. However, though the KV lumen area and the number of cilia were decreased in DFC *akap12β* morphants, the area for each cilium was insignificantly changed compared with DFC control morphants (Figs. 14-16). Together with that *akap12* was not expressed in KV lineage cells from bud stage (Fig. 6), it is hypothesized that the KV malformation in DFC *akap12β* morphants might be caused by the loss of *akap12β* during collective migration of DFCs. Since the pH3-positive DFCs in DFC *akap12β* morphants and DFC control morphants were not significantly different from each other (Fig. 17), I suppose that the reduction of Cdh1 level in DFC *akap12β* morphants might

result in a failure of cell collectivity within DFCs and the KV malformation (Fig. 19).

The role of *akap12* in regulating junction protein was previously reported in several papers. In blood-brain barrier formation, AKAP12 stimulated angiopoietin-1 expression in astrocytes and increased the expression of tight junction proteins (Lee et al., 2003). In addition, AKAP12 knockout mice showed the relatively less tight junction protein expressions in the fibrotic scar during the CNS repair process (Cha et al., 2014). Here, I found that *akap12* regulated the *cdh1* mRNA level as well as Cdh1 protein expression in DFCs, the migrating epithelial cells. However, the underlying mechanisms, how *akap12* regulate cdh1 mRNA expression, need to be further investigation.

Furthermore, I identified that *cldn5a* was highly expressed at the luminal surface of KV epithelial cells and sealed the paracellular spaces as a functional component of tight junction during KV lumen formation. DFC cluster, maintained by cadherin-based adherens junctions (Matsui et al., 2015), actively protrudes towards the vegetal pole showing filopodia and adheres to the overlying enveloping layer until polarization and detachment from the enveloping layer to form the rosette structure (Ablooglu et al., 2010; Oteiza et al., 2008). Then, the rosette structure is apically clustered and exhibits a centered lumen, called KV. These results revealed that *cldn5a* was expressed from the bud stages and was abundantly localized at the luminal surface of KV when the DFC detached from the enveloping layer and underwent apical clustering and lumen formation (Fig. 29). In addition, *sox17:egfp*-positive cells in DFC *cldn5a* morphants at 75% epiboly were grouped together without fragmentation and the number of *sox17:egfp*-positive cells at the bud stage was

similar (Fig. 40). Thus, I assumed that *cldn5a* plays a role in sealing the KV luminal surface, but not in maintaining DFC cluster, nor in DFC-enveloping layer adhesion.

KV lumen is expanded by fluid influx through the Cftr channel, and the proper size of the KV lumen is important for left-right asymmetric development (Ellertsdottir et al., 2006; Gokey et al., 2016; Navis et al., 2013; Roxo-Rosa et al., 2015). It was reported that not only the reduced size of KV lumen, but also over-inflation of the KV lumen by reinforced activation of the Cftr channel disrupted regional cell shape changes of KV epithelial cells and caused defective left-right asymmetry (Compagnon et al., 2014; Gokey et al., 2016; Navis et al., 2013; Roxo-Rosa et al., 2015). In this regard, *cldn5a* downregulation resulted in a decreased KV lumen area (Fig. 43). Moreover, combined treatment with forskolin and IBMX, which increases the fluid influx through the Cftr channel, was ineffective to restore the KV lumen size in DFC *cldn5a* morphants (Fig. 45). It suggests that the fluid leaked through the defective intercellular space between the KV epithelial cells in DFC *cldn5a* morphants, although a more direct way such as dextran injection into KV to probe the loss of paracellular tightness in DFC *cldn5a* morphants is needed. Nevertheless, the incomplete, but partially formed KV lumen in DFC *cldn5a* morphants still persisted in the absence of paracellular tightness. I suspect that regional cell shape changes by extracellular matrix accumulation and *rock2b*-mediated cytoskeletal rearrangement led to hollow spaces between the cells (Compagnon et al., 2014; Wang et al., 2011; Wang et al., 2012). In addition, normal localization of ZO-1, the cytoplasmic adaptor protein for the tight junction component, at the luminal surface in DFC *cldn5a* morphants implies

the presence of another tight junction protein, which sustains the partially formed lumen between the weakly adhered cells.

As a ciliated organ, the number of motile monocilia within the KV is important for the functional signal generation. More than 30 cilia are needed to drive sufficient force of fluid flow and induce the early left-right markers, *dand5* and *spaw* (Sampaio et al., 2014; Smith et al., 2014). In addition, the adequate length of cilia is important for left-right asymmetric development, as longer or shorter cilia lengths disrupt organ laterality by regulating the cilia beating frequency (Lopes et al., 2010; Pintado et al., 2017; Sampaio et al., 2014). Although ciliogenesis occurs by complicated mechanisms, including FGF, Hedgehog, Notch, and nc-Wnt signaling pathways (Matsui and Bessho, 2012), Navis et al. (Navis et al., 2013) suggested that the generation of cilia is not related to lumen expansion. In their model, *cftr* mutant, cilia were generated within the center of the KV lumen even though the luminal space was undetectable. In this case, a decreased number, but normal length of cilia was located near the under-inflated lumen in DFC *cldn5a* morphants (Fig. 39). This discrepancy could be interpreted as ciliogenesis is related to apical-basal polarity, rather than sufficient space. Considering that neighboring KV epithelial cells lose their paracellular tightness, I suspect that a part of non-lumen-facing KV cells might lose their apical-basal polarity in DFC *cldn5a* morphants. However, the relevance between lumen formation and the potency of ciliogenesis needs further elucidation.

As a consequence of the reduced number of cilia within the defective KV lumen, *dand5* was aberrantly expressed in DFC *cldn5a* morphants (Fig. 38), indicating KV dysfunction. Besides, the expression of *dand5* was decreased in

DFC *cldn5a* morphants, though cilia-driven fluid dynamics were inversely related to *dand5* expression (Sampaio et al., 2014). I suspect that this might be the combined result of defective KV with high permeability and a decreased number of cilia. One possible explanation is that the initial transcription of *dand5* might be reduced due to the reduction of KV lumen-facing cells. Another one is that leaking fluid might affect the degradation of *dand5*. In any case, the expression of *spaw* was not fully restricted to the left LPM showing bilateral or right-sided patterns, as a consequence of the aberrant expression of *dand5*, and the heart laterality was disrupted in DFC *cldn5a* morphants.

In consequence of abnormal KV lumen and decreased number of cilia in KV, *dand5* was aberrantly expressed in DFC *akap12β* and *cldn5a* morphants, depicting that KV was malfunctional. Thus, the expression of *nodal*-related gene, *spaw,* was not fully restricted to the left LPM showing bilateral or right-sided patterns, and the heart laterality was disrupted in DFC *akap12β* and *cldn5a* morphants.

Taken together, I identified that akap12 supports cell collectivity within DFCs by regulating *cdh1* expression, and *cldn5a* tightly seals the luminal surface of KV as the functional tight junction component during KV lumen formation. Thus, these results would give rise to the advanced understandings about KV lumen formation and organ laterality

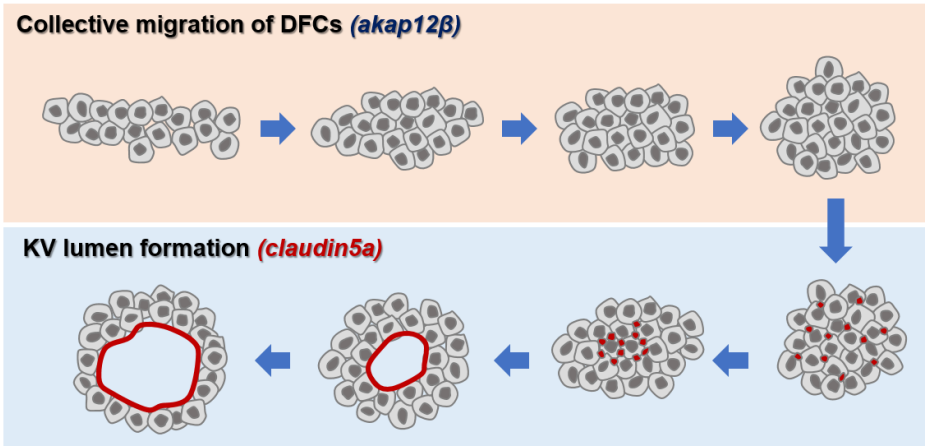

Figure 50. Schematic depiction of the role of *akap12β* and *cldn5a* in KV development.

REFERENCES

Ablooglu, A.J., Tkachenko, E., Kang, J., and Shattil, S.J. (2010). Integrin alphaV is necessary for gastrulation movements that regulate vertebrate body asymmetry. Development (Cambridge, England) *137*, 3449-3458.

Amack, J.D., and Yost, H.J. (2004). The T box transcription factor no tail in ciliated cells controls zebrafish left-right asymmetry. Current biology : CB *14*, 685-690.

Baker, K., Holtzman, N.G., and Burdine, R.D. (2008). Direct and indirect roles for Nodal signaling in two axis conversions during asymmetric morphogenesis of the zebrafish heart. Proceedings of the National Academy of Sciences of the United States of America *105*, 13924-13929.

Bisgrove, B.W., Makova, S., Yost, H.J., and Brueckner, M. (2012). RFX2 is essential in the ciliated organ of asymmetry and an RFX2 transgene identifies a population of ciliated cells sufficient for fluid flow. Developmental biology *363*, 166-178.

Bisgrove, B.W., Snarr, B.S., Emrazian, A., and Yost, H.J. (2005). Polaris and Polycystin-2 in dorsal forerunner cells and Kupffer's vesicle are required for specification of the zebrafish left-right axis. Developmental biology *287*, 274-288.

Bussmann, J., and Schulte-Merker, S. (2011). Rapid BAC selection for tol2-mediated transgenesis in zebrafish. Development (Cambridge, England) *138*, 4327-4332.

Ceccaldi, P.F., Carre-Pigeon, F., Youinou, Y., Delepine, B., Bryckaert, P.E., Harika, G., Quereux, C., and Gaillard, D. (2004). [Kartagener's syndrome and infertility: observation, diagnosis and treatment]. Journal de gynecologie, obstetrique et biologie de la reproduction *33*, 192-194.

Cereijido, M., Contreras, R.G., and Shoshani, L. (2004). Cell adhesion, polarity, and epithelia in the dawn of metazoans. Physiological reviews *84*, 1229-1262.

Cha, J.H., Wee, H.J., Seo, J.H., Ahn, B.J., Park, J.H., Yang, J.M., Lee, S.W., Kim, E.H., Lee, O.H., Heo, J.H., *et al.* (2014). AKAP12 mediates barrier functions of fibrotic scars during CNS repair. PloS one *9*, e94695.

Compagnon, J., Barone, V., Rajshekar, S., Kottmeier, R., Pranjic-Ferscha, K., Behrndt, M., and Heisenberg, C.P. (2014). The notochord breaks bilateral symmetry by controlling cell shapes in the zebrafish laterality organ. Developmental cell *31*, 774-783.

Cooper, I., Cohen-Kashi-Malina, K., and Teichberg, V.I. (2011). Claudin-5 expression in in vitro models of the blood-brain barrier. Methods in molecular biology (Clifton, NJ) *762*, 347-354.

de Campos-Baptista, M.I., Holtzman, N.G., Yelon, D., and Schier, A.F. (2008). Nodal signaling promotes the speed and directional movement of cardiomyocytes in zebrafish. Developmental dynamics : an official publication of the American Association of Anatomists *237*, 3624-3633.

Ellertsdottir, E., Ganz, J., Durr, K., Loges, N., Biemar, F., Seifert, F., Ettl, A.K., Kramer-Zucker, A.K., Nitschke, R., and Driever, W. (2006). A mutation in the zebrafish Na,K-ATPase subunit atp1a1a.1 provides genetic evidence that the sodium potassium pump contributes to left-right asymmetry downstream or in parallel to nodal flow. Developmental dynamics : an official publication of the American Association of Anatomists *235*, 1794-1808.

Essner, J.J., Amack, J.D., Nyholm, M.K., Harris, E.B., and Yost, H.J. (2005). Kupffer's vesicle is a ciliated organ of asymmetry in the zebrafish embryo that initiates left-right development of the brain, heart and gut. Development (Cambridge, England) *132*, 1247-1260.

Farquhar, M.G., and Palade, G.E. (1963). Junctional complexes in various epithelia. The Journal of cell biology *17*, 375-412.

Fliegauf, M., Benzing, T., and Omran, H. (2007). When cilia go bad: cilia defects and ciliopathies. Nat Rev Mol Cell Biol *8*, 880-893.

Francescatto, L., Rothschild, S.C., Myers, A.L., and Tombes, R.M. (2010). The activation of membrane targeted CaMK-II in the zebrafish Kupffer's vesicle is required for left-right asymmetry. Development (Cambridge, England) *137*,

2753-2762.
Gokey, J.J., Ji, Y., Tay, H.G., Litts, B., and Amack, J.D. (2016). Kupffer's vesicle size threshold for robust left-right patterning of the zebrafish embryo. Developmental dynamics : an official publication of the American Association of Anatomists *245*, 22-33.
Hashimoto, H., Rebagliati, M., Ahmad, N., Muraoka, O., Kurokawa, T., Hibi, M., and Suzuki, T. (2004). The Cerberus/Dan-family protein Charon is a negative regulator of Nodal signaling during left-right patterning in zebrafish. Development (Cambridge, England) *131*, 1741-1753.
Horne-Badovinac, S., Rebagliati, M., and Stainier, D.Y. (2003). A cellular framework for gut-looping morphogenesis in zebrafish. Science *302*, 662-665.
Jao, L.E., Wente, S.R., and Chen, W. (2013). Efficient multiplex biallelic zebrafish genome editing using a CRISPR nuclease system. Proceedings of the National Academy of Sciences of the United States of America *110*, 13904-13909.
Jeong, J.Y., Kwon, H.B., Ahn, J.C., Kang, D., Kwon, S.H., Park, J.A., and Kim, K.W. (2008). Functional and developmental analysis of the blood-brain barrier in zebrafish. Brain research bulletin *75*, 619-628.
Jia, W., Lu, R., Martin, T.A., and Jiang, W.G. (2014). The role of claudin-5 in blood-brain barrier (BBB) and brain metastases (review). Molecular medicine reports *9*, 779-785.
Jurynec, M.J., Xia, R., Mackrill, J.J., Gunther, D., Crawford, T., Flanigan, K.M., Abramson, J.J., Howard, M.T., and Grunwald, D.J. (2008). Selenoprotein N is required for ryanodine receptor calcium release channel activity in human and zebrafish muscle. Proceedings of the National Academy of Sciences of the United States of America *105*, 12485-12490.
Kim, H.H., Kim, J.G., Jeong, J., Han, S.Y., and Kim, K.W. (2014). Akap12 is essential for the morphogenesis of muscles involved in zebrafish locomotion. Differentiation; research in biological diversity *88*, 106-116.
Kok, F.O., Shin, M., Ni, C.W., Gupta, A., Grosse, A.S., van Impel, A., Kirchmaier,

B.C., Peterson-Maduro, J., Kourkoulis, G., Male, I.*, et al.* (2015). Reverse genetic screening reveals poor correlation between morpholino-induced and mutant phenotypes in zebrafish. Developmental cell *32*, 97-108.

Kramer-Zucker, A.G., Olale, F., Haycraft, C.J., Yoder, B.K., Schier, A.F., and Drummond, I.A. (2005). Cilia-driven fluid flow in the zebrafish pronephros, brain and Kupffer's vesicle is required for normal organogenesis. Development (Cambridge, England) *132*, 1907-1921.

Krock, B.L., and Perkins, B.D. (2014). The Par-PrkC polarity complex is required for cilia growth in zebrafish photoreceptors. PloS one *9*, e104661.

Kwon, H.B., Choi, Y.K., Lim, J.J., Kwon, S.H., Her, S., Kim, H.J., Lim, K.J., Ahn, J.C., Kim, Y.M., Bae, M.K.*, et al.* (2012). AKAP12 regulates vascular integrity in zebrafish. Experimental & molecular medicine *44*, 225-235.

Lee, S.W., Kim, W.J., Choi, Y.K., Song, H.S., Son, M.J., Gelman, I.H., Kim, Y.J., and Kim, K.W. (2003). SSeCKS regulates angiogenesis and tight junction formation in blood-brain barrier. Nature medicine *9*, 900-906.

Lenhart, K.F., Lin, S.Y., Titus, T.A., Postlethwait, J.H., and Burdine, R.D. (2011). Two additional midline barriers function with midline lefty1 expression to maintain asymmetric Nodal signaling during left-right axis specification in zebrafish. Development (Cambridge, England) *138*, 4405-4410.

Lin, A.E., Krikov, S., Riehle-Colarusso, T., Frias, J.L., Belmont, J., Anderka, M., Geva, T., Getz, K.D., and Botto, L.D. (2014). Laterality defects in the national birth defects prevention study (1998-2007): birth prevalence and descriptive epidemiology. American journal of medical genetics Part A *164a*, 2581-2591.

Liu, D.W., Hsu, C.H., Tsai, S.M., Hsiao, C.D., and Wang, W.P. (2011). A variant of fibroblast growth factor receptor 2 (Fgfr2) regulates left-right asymmetry in zebrafish. PloS one *6*, e21793.

Long, S., Ahmad, N., and Rebagliati, M. (2003). The zebrafish nodal-related gene southpaw is required for visceral and diencephalic left-right asymmetry. Development (Cambridge, England) *130*, 2303-2316.

Lopes, S.S., Lourenco, R., Pacheco, L., Moreno, N., Kreiling, J., and Saude, L. (2010). Notch signalling regulates left-right asymmetry through ciliary length

control. Development (Cambridge, England) *137*, 3625-3632.
Matsui, T., and Bessho, Y. (2012). Left-right asymmetry in zebrafish. Cellular and molecular life sciences : CMLS *69*, 3069-3077.
Matsui, T., Ishikawa, H., and Bessho, Y. (2015). Cell collectivity regulation within migrating cell cluster during Kupffer's vesicle formation in zebrafish. Frontiers in cell and developmental biology *3*, 27.
McComb, P., Langley, L., Villalon, M., and Verdugo, P. (1986). The oviductal cilia and Kartagener's syndrome. Fertility and sterility *46*, 412-416.
Nakamura, T., and Hamada, H. (2012). Left-right patterning: conserved and divergent mechanisms. Development (Cambridge, England) *139*, 3257-3262.
Navis, A., Marjoram, L., and Bagnat, M. (2013). Cftr controls lumen expansion and function of Kupffer's vesicle in zebrafish. Development (Cambridge, England) *140*, 1703-1712.
Nitta, T., Hata, M., Gotoh, S., Seo, Y., Sasaki, H., Hashimoto, N., Furuse, M., and Tsukita, S. (2003). Size-selective loosening of the blood-brain barrier in claudin-5-deficient mice. The Journal of cell biology *161*, 653-660.
Novodvorsky, P., Watson, O., Gray, C., Wilkinson, R.N., Reeve, S., Smythe, C., Beniston, R., Plant, K., Maguire, R., A, M.K.R.*, et al.* (2015). klf2ash317 Mutant Zebrafish Do Not Recapitulate Morpholino-Induced Vascular and Haematopoietic Phenotypes. PloS one *10*, e0141611.
Ohtsuki, S., Sato, S., Yamaguchi, H., Kamoi, M., Asashima, T., and Terasaki, T. (2007). Exogenous expression of claudin-5 induces barrier properties in cultured rat brain capillary endothelial cells. Journal of cellular physiology *210*, 81-86.
Ohtsuki, S., Yamaguchi, H., Katsukura, Y., Asashima, T., and Terasaki, T. (2008). mRNA expression levels of tight junction protein genes in mouse brain capillary endothelial cells highly purified by magnetic cell sorting. Journal of neurochemistry *104*, 147-154.
Oishi, I., Kawakami, Y., Raya, A., Callol-Massot, C., and Izpisua Belmonte, J.C. (2006). Regulation of primary cilia formation and left-right patterning in zebrafish by a noncanonical Wnt signaling mediator, duboraya. Nature

genetics *38*, 1316-1322.
Oteiza, P., Koppen, M., Concha, M.L., and Heisenberg, C.P. (2008). Origin and shaping of the laterality organ in zebrafish. Development (Cambridge, England) *135*, 2807-2813.
Oteiza, P., Koppen, M., Krieg, M., Pulgar, E., Farias, C., Melo, C., Preibisch, S., Muller, D., Tada, M., Hartel, S., *et al.* (2010). Planar cell polarity signalling regulates cell adhesion properties in progenitors of the zebrafish laterality organ. Development (Cambridge, England) *137*, 3459-3468.
Pintado, P., Sampaio, P., Tavares, B., Montenegro-Johnson, T.D., Smith, D.J., and Lopes, S.S. (2017). Dynamics of cilia length in left-right development. Royal Society open science *4*, 161102.
Place, E.S., and Smith, J.C. (2017). Zebrafish atoh8 mutants do not recapitulate morpholino phenotypes. PloS one *12*, e0171143.
Radeva, M.Y., Kugelmann, D., Spindler, V., and Waschke, J. (2014). PKA compartmentalization via AKAP220 and AKAP12 contributes to endothelial barrier regulation. PloS one *9*, e106733.
Rossi, A., Kontarakis, Z., Gerri, C., Nolte, H., Holper, S., Kruger, M., and Stainier, D.Y. (2015). Genetic compensation induced by deleterious mutations but not gene knockdowns. Nature *524*, 230-233.
Roxo-Rosa, M., Jacinto, R., Sampaio, P., and Lopes, S.S. (2015). The zebrafish Kupffer's vesicle as a model system for the molecular mechanisms by which the lack of Polycystin-2 leads to stimulation of CFTR. Biology open *4*, 1356-1366.
Sampaio, P., Ferreira, R.R., Guerrero, A., Pintado, P., Tavares, B., Amaro, J., Smith, A.A., Montenegro-Johnson, T., Smith, D.J., and Lopes, S.S. (2014). Left-right organizer flow dynamics: how much cilia activity reliably yields laterality? Developmental cell *29*, 716-728.
Schottenfeld, J., Sullivan-Brown, J., and Burdine, R.D. (2007). Zebrafish curly up encodes a Pkd2 ortholog that restricts left-side-specific expression of southpaw. Development (Cambridge, England) *134*, 1605-1615.
Smith, D.J., Montenegro-Johnson, T.D., and Lopes, S.S. (2014). Organized

chaos in Kupffer's vesicle: how a heterogeneous structure achieves consistent left-right patterning. Bioarchitecture *4*, 119-125.

Smith, K.A., Noel, E., Thurlings, I., Rehmann, H., Chocron, S., and Bakkers, J. (2011). Bmp and nodal independently regulate lefty1 expression to maintain unilateral nodal activity during left-right axis specification in zebrafish. PLoS genetics *7*, e1002289.

Streb, J.W., Kitchen, C.M., Gelman, I.H., and Miano, J.M. (2004). Multiple promoters direct expression of three AKAP12 isoforms with distinct subcellular and tissue distribution profiles. The Journal of biological chemistry *279*, 56014-56023.

Wang, G., Cadwallader, A.B., Jang, D.S., Tsang, M., Yost, H.J., and Amack, J.D. (2011). The Rho kinase Rock2b establishes anteroposterior asymmetry of the ciliated Kupffer's vesicle in zebrafish. Development (Cambridge, England) *138*, 45-54.

Wang, G., Manning, M.L., and Amack, J.D. (2012). Regional cell shape changes control form and function of Kupffer's vesicle in the zebrafish embryo. Developmental biology *370*, 52-62.

Wang, X., and Yost, H.J. (2008). Initiation and propagation of posterior to anterior (PA) waves in zebrafish left-right development. Developmental dynamics : an official publication of the American Association of Anatomists *237*, 3640-3647.

Weiser, D.C., Pyati, U.J., and Kimelman, D. (2007). Gravin regulates mesodermal cell behavior changes required for axis elongation during zebrafish gastrulation. Genes & development *21*, 1559-1571.

Zhang, J., Jiang, Z., Liu, X., and Meng, A. (2016). Eph/ephrin signaling maintains the boundary of dorsal forerunner cell cluster during morphogenesis of the zebrafish embryonic left-right organizer. Development (Cambridge, England) *143*, 2603-2615.

Zhang, J., Piontek, J., Wolburg, H., Piehl, C., Liss, M., Otten, C., Christ, A., Willnow, T.E., Blasig, I.E., and Abdelilah-Seyfried, S. (2010). Establishment of a neuroepithelial barrier by Claudin5a is essential for zebrafish brain ventricular

lumen expansion. Proceedings of the National Academy of Sciences of the United States of America *107*, 1425-1430.
Zhang, M., Zhang, J., Lin, S.C., and Meng, A. (2012). beta-Catenin 1 and beta-catenin 2 play similar and distinct roles in left-right asymmetric development of zebrafish embryos. Development (Cambridge, England) *139*, 2009-2019.
Zihni, C., Mills, C., Matter, K., and Balda, M.S. (2016). Tight junctions: from simple barriers to multifunctional molecular gates. Nat Rev Mol Cell Biol *17*, 564-580.

요약 (국문초록)

척추동물에서 기관이 적절히 발생하기 위해서는 좌우 비대칭적인 발생이 필수적이다. Kupffer’s vesicle (KV)은 제브라피쉬에서 좌우비대칭을 관장하는 기관으로서, 적절히 팽창된 KV 내강은 비대칭적인 신호전달에 중요하다. KV는 초기 체절형성시기에 척삭의 말단부분에서 일시적으로 존재하며, 전구체인 Dorsal forerunner cell (DFC)로부터 형성된다. 이러한 DFC는 배아의 배순(embryonic shield)에서부터 꼬리싹(tail bud)으로 하나의 무리를 유지하며 이동 후, 상피화를 거쳐 내강을 형성하며, ion channel에 의한 유체의 유입으로 내강이 팽창되어 성숙한 KV가 완성된다. 이 후에, nodal 신호가 좌측 lateral plate mesoderm을 통해 기관 전구세포까지 전달되며, 기관의 편측성이 결정된다. 하지만, 이러한 KV의 형성과정에서 세포간 상호작용에 대한 메커니즘은 자세히 알려져 있지 않다. 본 연구에서는 *akap12*가 DFC에서 발현함을 확인하였고, *akap12β*의 발현을 저해한 제브라피쉬 배아에서 비정상적인 KV의 발생과 더불어 기관의 비대칭이 망가짐을 확인하였다. 또한, KV와 전구체세포에 특이적으로 *akap12β*를 저해한 morphant에서도 기관의 비대칭이 망가짐을 확인하였다. 또한, KV와 전구체세포에 특이적으로 *akap12β*를 저해한 morphant에서도 기관의 비대칭이 망가짐을 확인하였다. *akap12β* morphant에서는 KV 전구체 세포그룹인 DFC 무리 주위의 Cdh1의 발현이 감소하며,

DFC 무리가 파편화됨을 보였다. 이러한 결과로 보아, *akap12β*는 Cdh1의 발현을 조절함으로서 DFC세포들의 집합성을 유지하는 것으로 보인다. 더욱이 본 연구자는 KV을 구성하는 상피세포의 내강부위에서 *cldn5a*가 발현하며, KV의 내강을 치밀하게 밀봉하고 있음을 발견하였다. 또한 *cldn5a*의 발현을 저해한 제브라피쉬 배아에서 KV이 적절히 발생되지 못하고, 기관의 편측성이 망가짐을 확인하였다. 게다가 forskolin과 3-isobutyl-1-methylxanthine을 처리함으로써 KV 내강을 팽창을 강화시켜 보았으나, cldn5a morphant에서는 KV 내강의 크기가 커지지 못하였다. 하지만, mCherry-cldn5a mRNA를 morpholino와 동시에 주입한 배아에서 높은 비율로 KV 내강의 크기와 심장의 편측성이 회복되는 것을 확인하였다. 이러한 결과들은 *cldn5a*가 KV의 내강 팽창과 그로인한 좌우 비대칭적인 발생에 중요한 역할을 함을 보였다. 위 결과들을 토대로, 본 연구자는 *akap12β*가 Cdh1의 발현을 조절함으로서 KV의 전구체인 DFC 사이의 접착결합을 유지하며, cldn5a가 KV를 구성하는 상피세포를 치밀하게 밀봉하여 KV의 발생을 조절함을 제시하는 바이다.

주 요 어 : AKAP12; Claudin5; Kupffer’s vesicle; Dorsal forerunner cells; collective cell migration; lumen formation; zebrafish

학 번 : 2013-31372